Study of a pulsed LED set-up to characterise the light response of SiPM sensors for the EIC dRICH detector

Relatore:
Prof. Andrea Alici

Correlatore:
Dott. Roberto Preghenella

Presentata da:
Giulia Fazzino

Sommario

L'Electron Ion Collider (EIC) è un futuro acceleratore di particelle che ha l'obiettivo di approfondire le nostre conoscenze riguardo l'interazione forte, una delle quattro interazioni fondamentali della natura, attraverso collisioni di elettroni su nuclei e protoni. L'infrastruttura del futuro detector comprende un sistema d'identificazione basato sull'emissione di luce Cherenkov, un fenomeno che permette di risalire alla massa delle particelle. Una delle configurazioni prese in considerazione per questo sistema è il dual-radiator RICH, basato sulla presenza di due radiatori all'esterno dei quali si trovano dei fotorivelatori. Un'opzione per questi sensori sono i fotorivelatori al silicio SiPM, oggetto di questo lavoro di tesi.

L'obiettivo dell'attività è lo studio di un set-up per la caratterizzazione della risposta di sensori SiPM a basse temperature, illuminati attraverso un LED. Dopo un'analisi preliminare per determinare le condizioni di lavoro, si è trovato che la misura è stabile entro un errore del 3.5%.

Abstract

The Electron Ion Collider (EIC) is a future particle accelerator which aims to deepen our knowledge on strong interaction, one of the four fundamentals interactions in nature, via collisions of electrons on nuclei and protons. The future detector infrastructure includes a particle identification system based on Cherenkov light emission, a phenomenon which can be used to measure particles mass. A configuration taken into consideration for this system is the dual-radiator RICH, based on two radiators surrounded by photo detectors. An option taken into consideration for these sensors are silicon photo detectors SiPM, subject of this thesis work.

The aim of the activity is studying a set-up to characterise the response of SiPM sensors lit by a LED and kept at low temperature. After a preliminary analysis to determine the working conditions, we found that the measurement is stable within an error of 3.5%.

Contents

Introduction

The Silicon Photomultiplier (SiPM) sensors are a kind of semiconductor photo detectors widely used in nuclear and subnuclear physics. They consist of an array of Single Photon Avalanche Diodes (SPADs) connected in parallel and consequently have single-photon resolution.

Currently, the SiPM are being considerate as an option for the particle identification system at the Electron Ion Collider, a future accelerator in the U.S.A. which is going to study the strong interaction. The detector will consist of three major systems: tracking and vertexing, particle identification and calorimetry. One of the options for the particle identification system is the dual-radiator RICH (dRICH), composed by two radiators of different materials surrounded by photo detectors, which will use the emission of Cherenkov light in order to measure the particles mass.

This work is centred around the study of a set-up used to characterise the light response of brand new SiPMs. The sensors have been used at low temperature, a condition necessary to limit thermal noise, and they have been lit using a pulsed LED.

In the following, Chapter 1 will provide further information on the EIC project, describing the object of studies of the experiment and its main scientific goals. The chapter will also provide a brief description of the future accelerator infrastructure, focusing mostly on the dRICH option.

Chapter 2 will firstly present the general operating principle of silicon detectors, based on the p-n junction. Afterwards, the chapter will analyse the operating principle of SiPM sensors, presenting their structure, the possible noise sources, their main characteristics and a possible way to improve their performance after radiation damage.

Lastly, Chapter 3 will describe the set-up used in this work, presenting the measurements carried out in order to characterise the light source and the results found for the measurements stability and homogeneity among different sensors.

Chapter 1

The Electron Ion Collider

The Electron Ion Collider (EIC) is a future particle accelerator which will be built in the United States of America (USA) in this decade. It will collide polarized beams of electrons and protons or ions at high intensity, granting access to deeper information on nuclear structure and strong nuclear force. The elementary constituents of nucleons are quarks and gluons, collectively called partons, held together by the strong nuclear force, one of the four fundamental interactions of the Standard Model. The action of this force is described by Quantum Chromodynamics (QCD) in terms of color charge which is a property of both quarks and gluons and comes in three types: green, red and blue, together with their anticolors. Strong nuclear interaction has 8 independent mediators, gluons, which carry a color-anticolor charge and hence have the possibility of interacting with each other, generating a significant part of the nucleon mass despite being the gluon itself massless.

One of the most peculiar features of QCD is "color confinement", a phenomenon by which color-charged particles cannot exist isolated, but rather tend to form colorless clusters via the process of hadronization. The number of valence quarks inside a hadron cannot be arbitrary, since the only possible values to form colorless hadrons are 2 (quark-antiquark) and 3 (quark-quark-quark), resulting respectively in particles called mesons and baryons. The proton and the neutron are examples of baryons. Along with valence quarks, which are relevant for determining quantum numbers, hadrons contain also virtual quark-antiquark pairs coming from gluon splitting called "sea quarks". These particles are not stable, since they tend to annihilate in a gluon.

Section 1.1 will give a brief introduction to the main questions about QCD and the constituents of the visible world that the EIC data will help to uncover.
Section 1.2 will describe the proposed accelerator and detector layouts.

1.1 Scientific goals

1.1.1 Multi-dimensional imaging of nucleons, nuclei and mesons

A deeper understanding of the inner structure of nucleons, nuclei and light mesons will be given by measurements of partons positions and momentum distributions.

Information on confined motion of partons is matched to transverse-momentum dependent parton distributions (TMDs), which depend on correlation between the motion of the partons, their spin and the parent nucleon's spin that may be caused by spin-orbit coupling. Currently only quarks transverse-momentum distribution has been studied, while there is no data for gluons or sea quarks. Throughout semi-inclusive deep inelastic scattering (DIS) measurements, which involve measuring momenta of both the scattered electron and the produced hadron, the EIC will expand our knowledge on partons motion.

As for spatial imaging, there is little known on partons distribution in the transversal spatial dimension inside a hadron. It can be studied via measurements of exclusive reactions, in which all final products are detected. Information on spatial distributions is encoded in generalized parton distribution functions (GPDs), which also provide insights into the angular momentum of nucleon constituents and the pressure inside the nucleon.

1.1.2 Nucleon properties

One of the questions the EIC will address is how properties such as spin and mass of nucleons arise from the ones of their constituents.

Mass In order to fully understand nucleon mass origin, it is fundamental to find out how this property emerges from strong interaction dynamics. In fact the Higgs mechanism, which gives mass to the constituents of matter, can only be responsible for a small fraction of proton and nucleon mass. The EIC will provide insights on the QCD trace anomaly contribution to the total mass by measuring the cross-section of quarkonium production near threshold.

Spin In the past decades it has been shown that quarks and antiquarks can account only for $\sim 30\%$ of the proton spin, while the gluon contribution is not enough to be responsible alone of the missing $\sim 70\%$. This evidence suggests that total spin does not only depend on the spin of partons, but there is also an orbital angular momentum contribution. This effect is not easily quantifiable since the contribution of partons to the total spin is strongly dependent on their minimum momentum fraction x. In this context, EIC aims to quantify quarks and gluons spin more precisely by lowering the minimum accessible value of x by at least two orders of magnitude and widening the range of momentum transfer Q. DIS measurements will be carried on collisions of longitudinally

polarized beams of electrons and nucleons; a projection of how uncertainties on the spin of partons contribution would reduce with EIC experiments is shown in Figure 1.1.
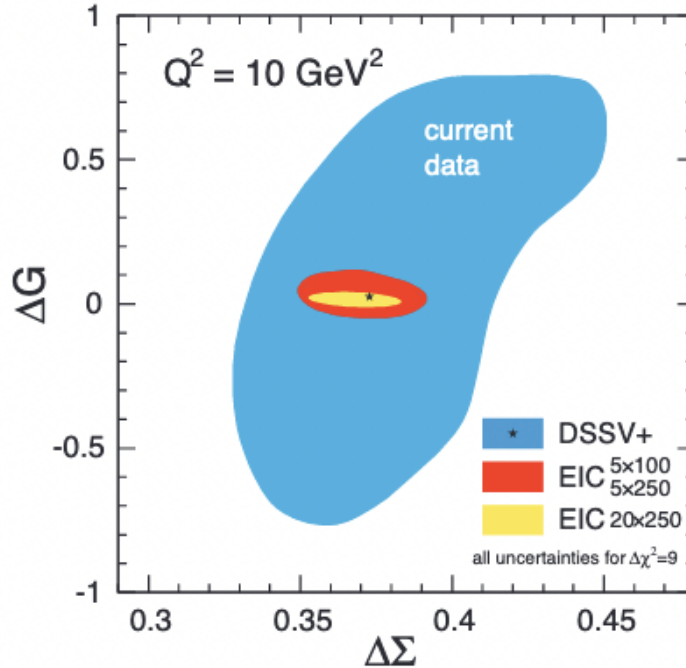

Figure 1.1: Reduction of uncertainties of gluons' helicity contribution (ΔG) versus quark's helicity contribution ($\Delta \Sigma$) to the proton spin in the region $x > 0.001$ for different center-of-mass energies, from [1].

1.1.3 Gluon saturation

A key goal of the EIC will be to observe a new state of nuclear matter: the Color Glass Condensate (CGC). The word "color" refers to the charge carried by gluons, "glass" represents disordered elements that slowly change their positions, and "condensate" means that the density is elevated.

This form of matter is the result of two opposite processes: while rising energy levels cause a growth in low-x gluons density, gluon-gluon recombination tends to limit this increase. When these two processes reach a balance, density is supposed to saturate, and new properties of hadronic matter would emerge.

The possibility of EIC of colliding heavy ions will make saturation scale more accessible, since the big number of quarks involved in the process will result in a decrease of the needed energy, as shown in Figure 1.2.
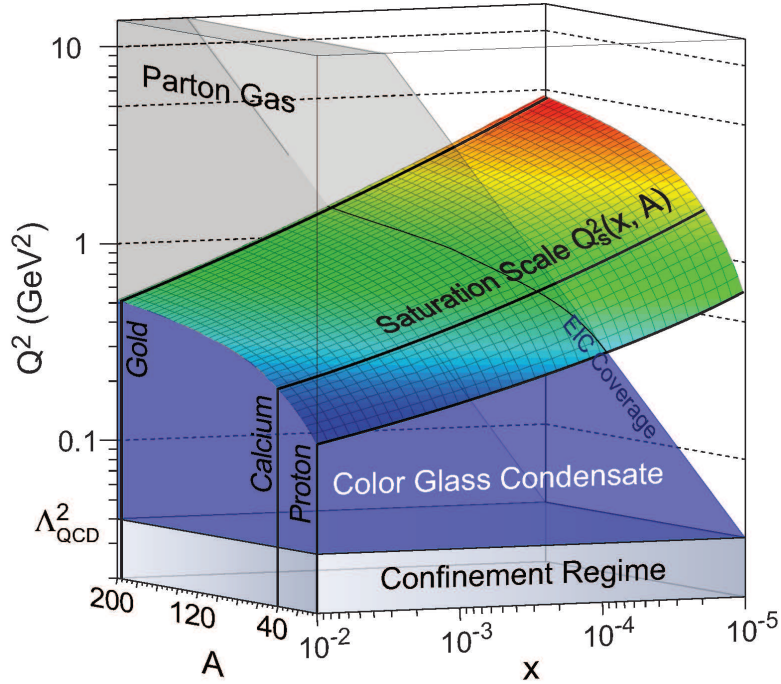
Figure 1.2: Dependence of the saturation scale on the nuclear mass number A, the minimum momentum fraction x and the resolution Q^2. For a fixed value of x, Q_S^2 is proportional to $A^{1/3}$.

1.1.4 Quarks and gluons in nuclei

Parton distributions At the moment our knowledge on parton distribution functions (PDFs) in nuclei is significantly limited with respect to our understanding of PDFs inside the proton. In particular, nuclear PDFs are not just a convolution of distributions in protons, and the ratio between these two quantities is significantly less than 1 for small values of x, an effect called "nuclear shadowing". The EIC high energy electron-nucleus collision will allow measurements of nuclear PDFs over a broad range of Q^2.

Charge propagation Electron-nucleus collision can also provide insights on how color charge carriers propagate and lose energy in cold QCD matter, and consequently expand our knowledge on hadronization.
When the virtual photon generated in a scattering event interacts with a quark from a nucleon, the latter receives a considerable amount of energy and will thus move inside the nucleon, interacting with its other constituents until it hadronizes, forming a colorless hadron. A schematic illustration of this interaction is shown in Figure 1.3.
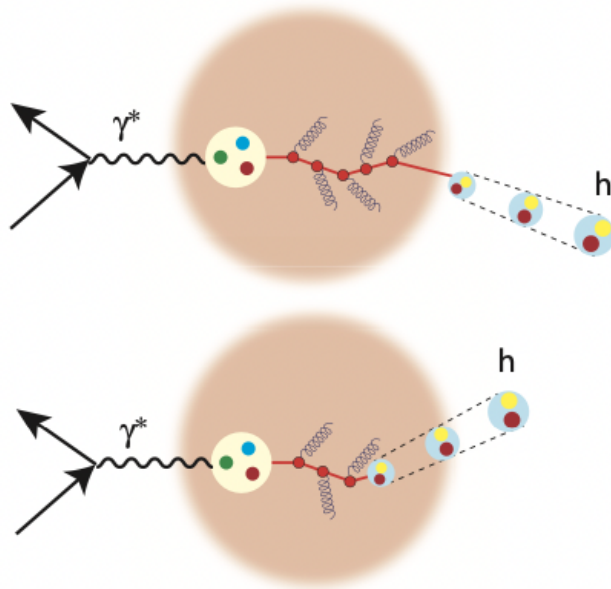
Figure 1.3: A schematic illustration of a parton moving inside a nucleus, the final hadron is produced outside (top) or inside (bottom) the nucleus.

1.2 Infrastructure

1.2.1 Accelerator

The EIC, shown in Figure 1.4, will collide beams of electrons on protons and nuclei using the existing Relativistic Heavy Ion Collider (RHIC) infrastructure at Brookhaven Nation Laboratory (BNL). The main features of the accelerator will be:

- beams of highly polarized electrons and nuclei;

- a vast range of different ions, from deuterons to heavy nuclei;

- at least one detector in an interaction region;

- a large center-of-mass energy range, from 20 to $100\,\mathrm{GeV}$, upgradable to $140\,\mathrm{GeV}$;

- high particle collision rate, with a luminosity of 10^{33} - 10^{34} $\mathrm{cm}^{-2}\mathrm{s}^{-1}$.
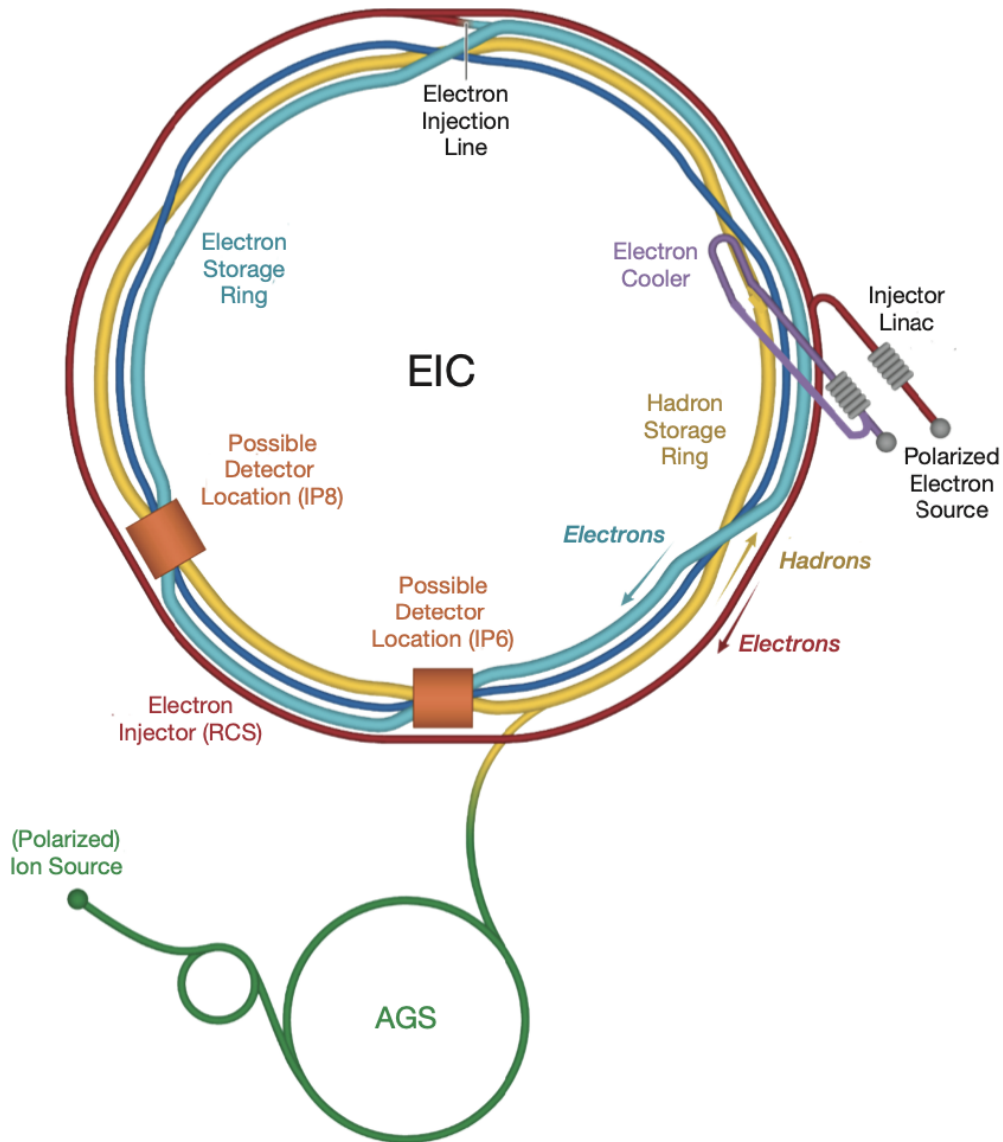
Figure 1.4: Schematic layout of the planned EIC accelerator based on the existing RHIC complex, from [2].

1.2.2 Detector Layout

The detector design in Figure 1.5 is centred around a solenoidal superconducting magnet, hence the major detector systems must be organized in a configuration with barrels and endcaps.

The innermost system takes care of tracking and vertexing. It will combine detector technologies based on semiconductors, where charged particles generate electron/hole pairs, and gases, where tracks cause ionization.

The second major system, providing particle identification, uses detectors which exploit time of flight measurements and Cherenkov light emission, a physical phenomenon happening when particles travel in a medium faster than the speed of light in the medium. The outermost major system, calorimetry, measures the energies of electrons, in the electromagnetic calorimeter, and hadrons, in the hadron calorimeter.
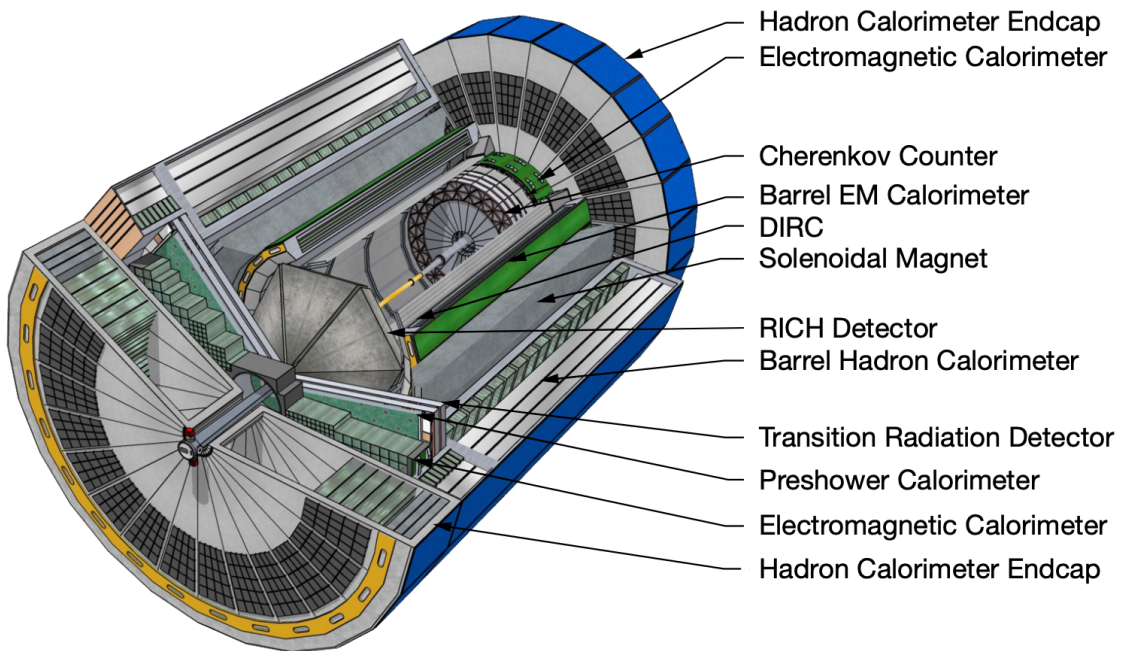

Figure 1.5: CAD model of an EIC detector concept, from [2].

1.2.3 Cherenkov particle identification: dual-radiator RICH

When charged particles move through a medium with a speed greater than light's phase velocity, they emit Cherenkov radiation. The direction θ of emitted light is correlated to particles speed by the relation $cos(\theta) = \frac{c}{nv}$, where n is the refraction index of the medium. Consequently, a measure of θ results in a measure of v, which can be put together with the information on momentum in order to determine the particle mass, identifying it. This kind of particle identification is only possible if v is above the threshold value $v_t = \frac{c}{n}$, subsequently materials with a low refraction index can not detect low momentum particles.

One of the configuration options for Cherenkov detectors considered is the dual Ring-Imaging Cherenkov detector (dRICH), schematically shown in Figure 1.6. It covers a wide momentum range by using two different radiators, and consequently two different refraction indexes: an aerogel radiator ($n = 1.02$) and a gas radiator (C_2F_6, $n = 1.0008$). Photosensors are located outside the acceptance; this results in moving the focal plane to a lower radiation zone, limiting background interference and allowing the possibility of using SiPM sensors for the readout.
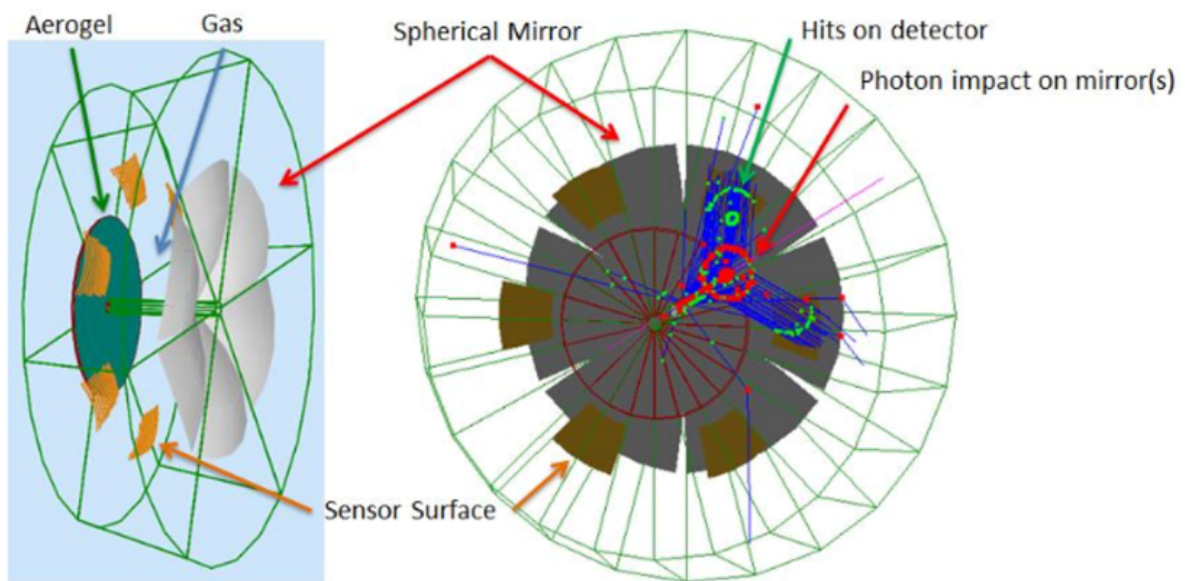

Figure 1.6: Dual RICH detector configuration, from [2].

Chapter 2

Silicon Detectors

Detectors based on semiconductors, such as silicon, are widely used in high-energy physics to detect charged particles or photons. Their working principle, which will be explained in Section 2.1, is based on the properties of p-n junctions.

Subsequently, Section 2.2 will focus on the Silicon Photomultiplier (SiPM), a specific type of silicon detector, presenting its main characteristics.

2.1 Operating principle

2.1.1 Semiconductors

Solid-state detectors are made using semiconductor materials whose atoms belong to the group IV of the periodic table.

Since atoms in crystals are close to each other their electronic levels tend to merge into two bands: the valence band and the conduction band, separated by an energy gap E_g. This structure is illustrated in Figure 2.1 (right). The main feature of semiconductors is that while they behave like insulators at very low temperatures, increasing thermal energy can cause some of the covalent bonds between the atoms to break, generating an electron-hole pair and thus enabling electrical conduction within the material. Usually the energy necessary to form an e-h pair is in the order of magnitude of $1\,\mathrm{eV}$, for instance for silicon at room temperature pair production requires an energy of $3.6\,\mathrm{eV}$.

In practical applications, semiconductors are often used in a doped structure, i.e. with some of their atoms replaced by atoms of the group III (acceptors) or V (donors). The presence of atoms with a different number of valence electrons leads to an excess of holes or electrons, thus doped materials are called respectively p-type or n-type semiconductors. From the energetic point of view, the presence of impurities within the crystal corresponds to an additional level inside the gap, as shown in Figure 2.1 (left).
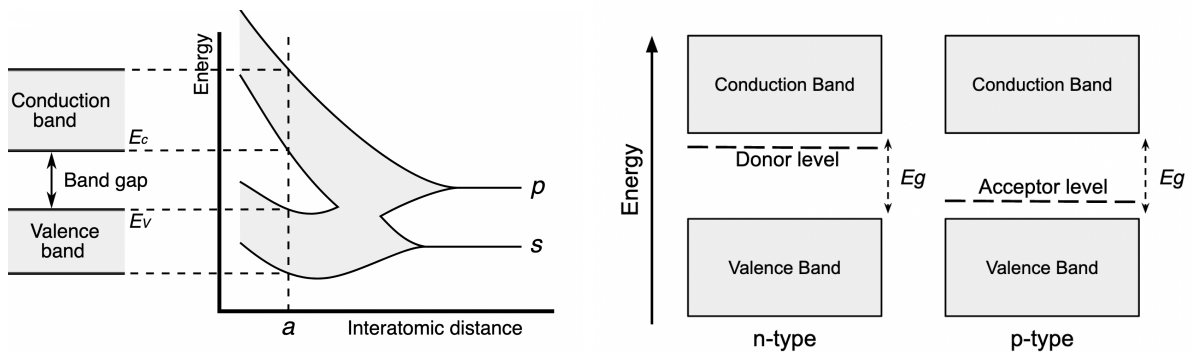
Figure 2.1: Right: illustration of how the band structure of a lattice emerges at low interatomic distances. Left: energy levels for a doped semiconductor.

2.1.2 The p-n junction

The basic structure of a silicon detector is the p-n junction: an interface between a p-type and an n-type semiconductor which conducts electrical current primarily in one direction. Due to the inhomogeneous distribution of the charge carriers, they will tend to diffuse from one region to the other, recombining near the junction and giving rise to an electric field that opposes the diffusion motion. When equilibrium is reached this process ends and the region near the junction, called "depletion region", is left devoid of mobile charges. Figure 2.2 displays how the dimension of the depletion region varies by applying an external voltage at the junction's edges. In forward bias (i.e. when the p-doped region is attached to the positive terminal of the voltage source) major carriers are able to reach the opposite region and neutralize its uncovered charges, reducing consequently the depletion region dimensions. In reverse bias, on the contrary, carriers are pulled away from the junction and the width of the depletion region increases.

Usually silicon detectors are operated in reverse bias. When an energetic particle travels through the detector it can generate an electron-hole pair which, under the influence of the depletion region's electric field, travel to the electrodes resulting in a measurable current.

The diode characteristic curve, depicted in Figure 2.3, shows that when the junction is used in reverse bias the current flow is almost zero. The absence of current is a consequence of the high electric field in the depletion region. This holds unless the intensity of the electric field reaches a critical level at which it breaks down the dielectric, causing an extremely rapid current increase. The condition for such phenomenon to happen is that the applied voltage reaches the breakdown value V_{BD}, which depends on the junction material and on the temperature, since the carriers mobility and the ionization rate are temperature dependent.
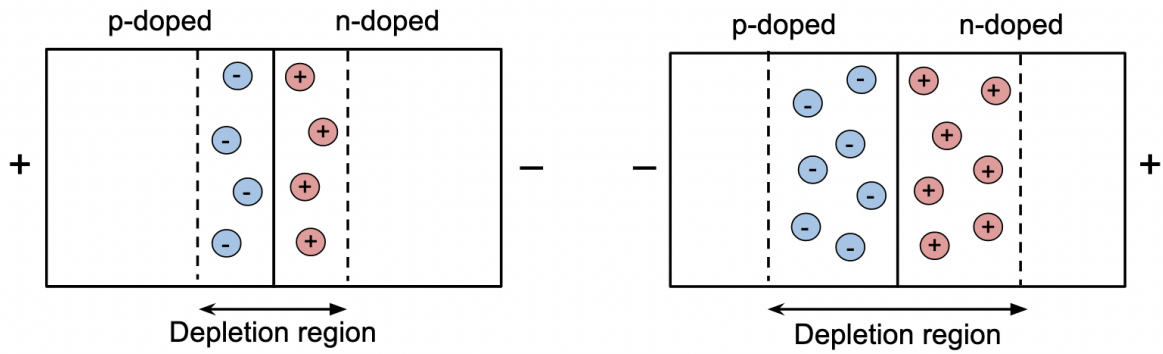
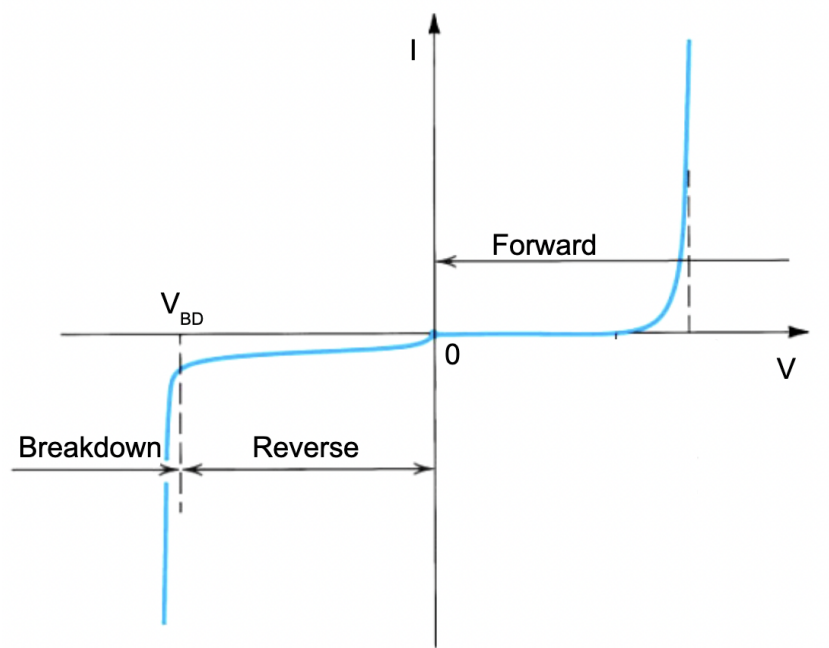Figure 2.2: A p-n junction in different polarizations regimes.

Figure 2.3: Characteristic curve of a polarized p-n junction (diode).

2.2 Silicon Photomultiplier

2.2.1 Single Photon Avalanche Diode (SPAD)

The Silicon Photomultiplier is an array of independent microcells consisting each of a SPAD sensor and a quenching circuit.

SPADs are photodiodes which use avalanche multiplication as internal gain mechanism: if the electric field in the depletion region is sufficiently intense, when a charge carrier is generated it gains enough kinetic energy to create secondary e-h pairs through a process called "impact ionization". In this way a single incident photon can trigger a self-sustaining avalanche process resulting in a macroscopic current flow.

The condition of high electric field is met by applying a reverse bias voltage V_{bias} above the breakdown voltage. Once the current flows the process does not stop unless the voltage is lowered below the breakdown value; this is done by a "quenching circuit". The diode then recharges back to the bias voltage and it is again able to detect photons. This working cycle is shown in Figure 2.4.
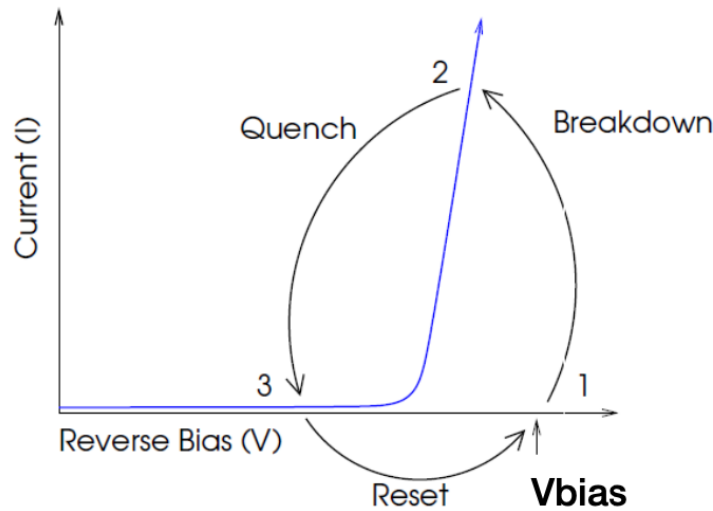

Figure 2.4: Breakdown, quench and reset of a SPAD working in Geiger mode, from [3].

A SPAD, the structure of which is illustrated in Figure 2.5, can be modeled as the circuit shown in Figure 2.6. The overall circuit consists of the series connection between the quenching circuit and the SPAD. The former is composed by a resistor R_q and a parasitic capacitance C_q in parallel, while the latter is the parallel of the internal resistance of the diode's depletion region R_d and its capacitance C_d, which is the sum of the SPAD area capacitance and other perimeter or parasitic capacitances. In the quiescent state the circuit's switch is open and the voltage on C_d is the applied voltage V_{bias}.

An avalanche-triggering event, which can be either a detected photon or a noise event, is modeled by closing the switch. This starts to discharge the diode's capacitor and causes a voltage drop in the node between C_d and C_q, while at the same time C_q charges via R_q. The total capacitance involved in the process is the sum of C_q and C_d, so the voltage discharge time is

$$\tau_d = R_d(C_q + C_d) \tag{2.1}$$

where the influence of R_q has been neglected because it is far more resistive than R_d. The discharge of C_d and recharge of C_q ends when the current flowing through the R_d reaches the minimum possible value to get a self sustainable avalanche, which is approximately

$$I_d = \frac{V_{ov}}{R_q + R_d} \sim \frac{V_{ov}}{R_q} \tag{2.2}$$

where V_{ov} is the overvoltage $V_{ov} = V_{bias} - V_{BD}$. At this point the avalanche is quenched and the cell returns to its initial conditions within a recharge time

$$\tau_r = R_q(C_q + C_d) \tag{2.3}$$

The gain G of the SPAD quantifies the number of charge carriers generated per event, it can be defined as the ratio between the total charge involved in the avalanche and the elementary charge e

$$G = \frac{\text{avalanche charge}}{e} = \frac{V_{ov}(C_q + C_d)}{e} \tag{2.4}$$

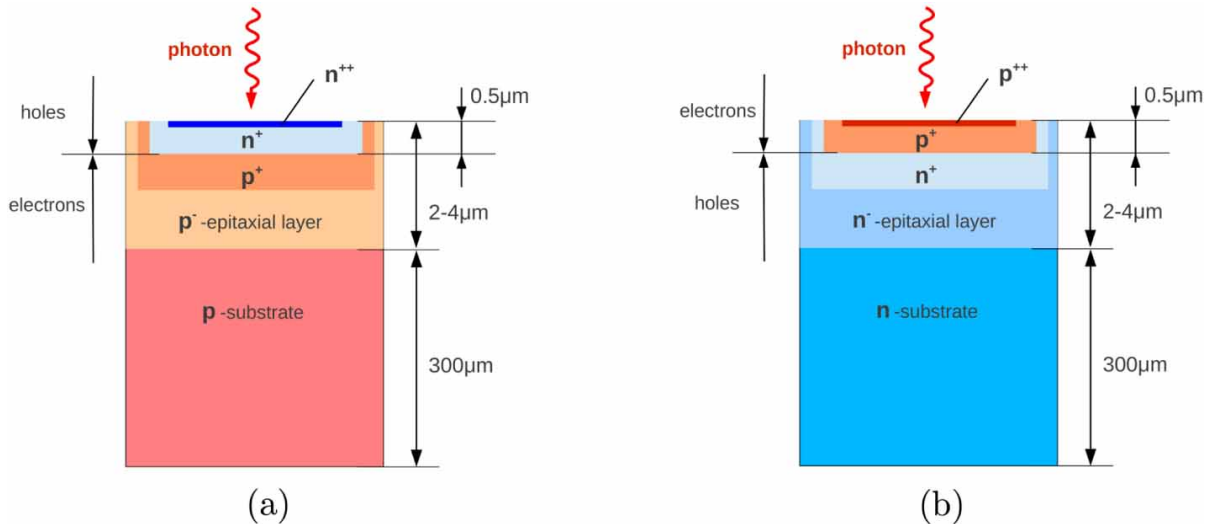and it is typically in the order of 10^5 to 10^7.

Figure 2.5: Structure of an n-doped on p-doped (left) and a p-doped on n-doped (right) SPAD, from [4].
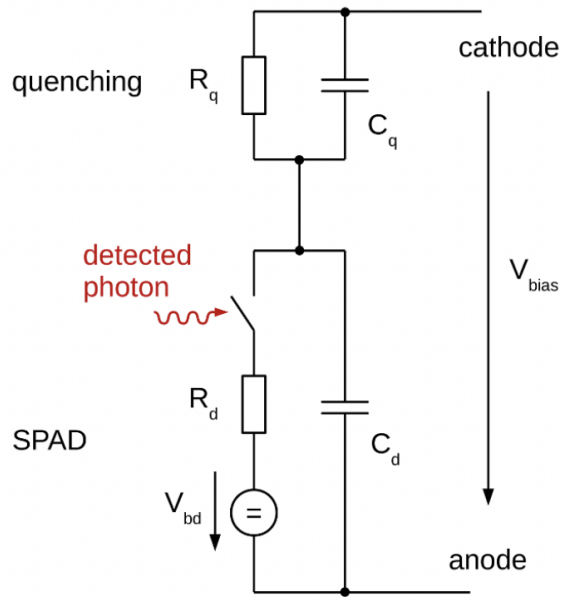
Figure 2.6: SPAD equivalent circuit, from [4].

2.2.2 Analog SiPM

A SiPM, shown in Figure 2.7, typically has a dimension in the order of magnitude of a few millimetres and it integrates several microcells, which size usually varies between 20x20 µm and 50x50 µm, connected in parallel.
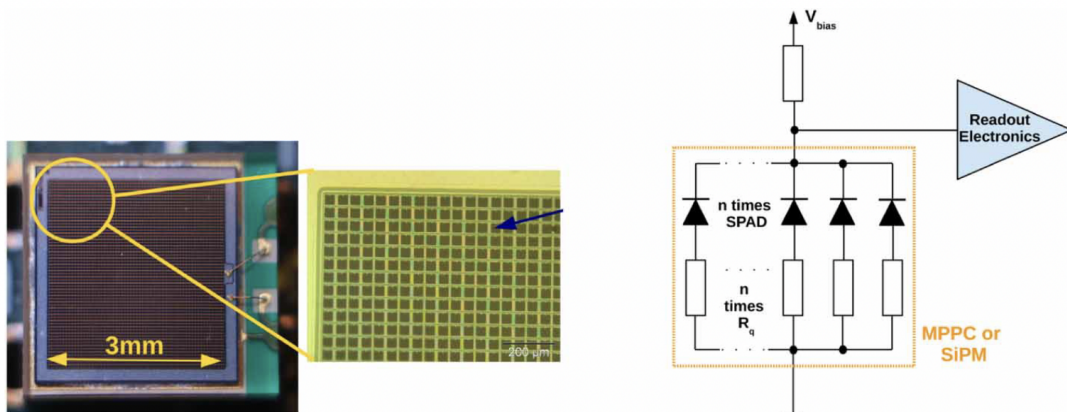

Figure 2.7: Picture (right) and equivalent circuit (left) of an analog SiPM, from [4].

The parallel connection ensures that the total output current is the sum of the photocurrents of each fired SPAD, resulting in a discrete output dependent on the number

of triggering events similar to the one depicted in Figure 2.8. However, since each SPAD has a certain dead time after being fired, it is not possible to distinguish whether a microcell has detected one or more photons.
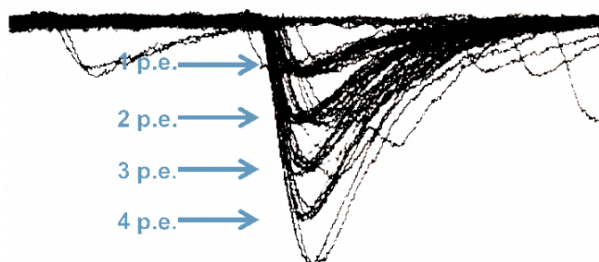

Figure 2.8: Oscilloscope shot of the discrete output of a SiPM, from [3].

2.2.3 Noise

In SiPM detectors there are two possible kinds of noise sources: primary and correlated (or secondary). The output signal for some examples of these noise contributions in an analog SiPM is shown in Figure 2.9.

The main source of primary noise is the dark count rate (DCR), caused by thermally generated electron-hole pairs. Secondary noise events are the ones triggered by a primary event, which could be either a detected photon or a noise signal. Two examples of correlated noise, described in the following paragraphs and schematically illustrated in Figure 2.10, are the afterpulse and the crosstalk.
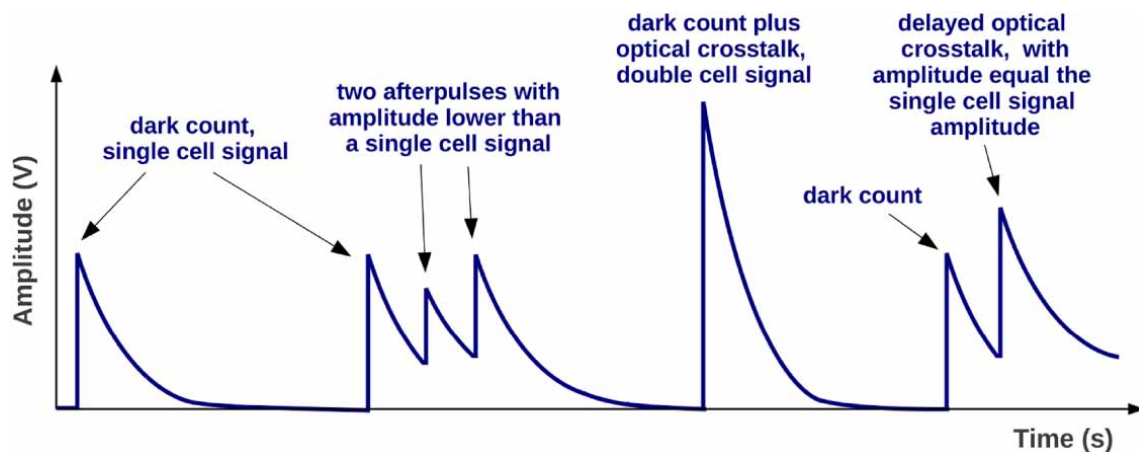

Figure 2.9: Signal amplitude of the three different kinds of noise (DCR, afterpulse and crosstalk) observable on an analog SiPM, from [4].
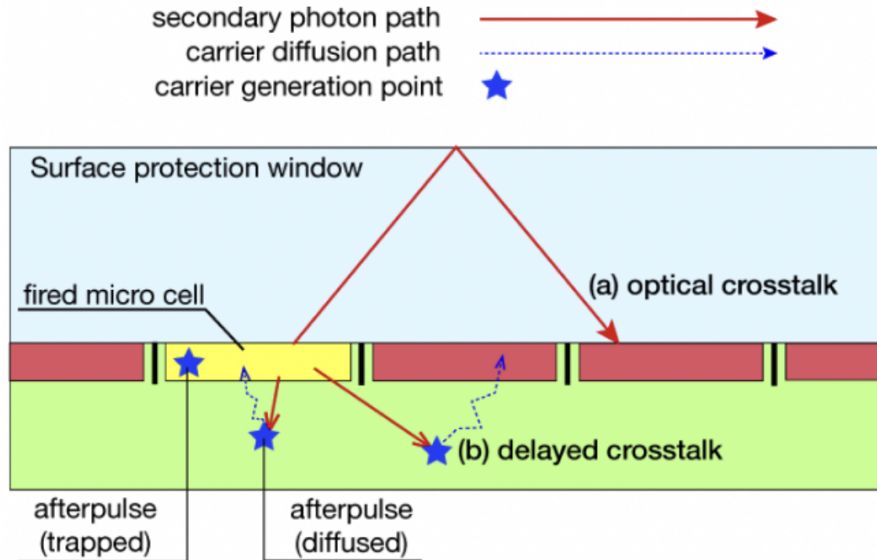
Figure 2.10: Schematic view of afterpulse and crosstalk. Path (a) shows external crosstalk, it can be noted that the fired cells are not adjacent, while path (b) shows delayed crosstalk. From [5].

Dark count rate The DCR is a kind of noise due to the presence of thermally generated carrier pairs that can trigger the avalanche process, producing a signal that cannot be distinguished from the one of a detected photon. This effect strongly depends on temperature, as the dark current generally halves for each $10\,\mathrm{K}$ drop in temperature [4]. It can be improved via specific production processes and material purity.

Afterpulse The afterpulse is caused by the trapping and release of charges in the region with intense electric field. It typically occurs within the same cell of the primary avalanche and it is characterized by a signal amplitude lower than that of the primary event. Afterpulsing probability is proportional to the number of traps and the release time constant compared to the recharge time of the SPAD (Equation 2.3), hence it is reduced in sensors with a long recharge time.
Aside from trapped charges, afterpulse can be also caused by secondary photons produced during the avalanche, the amount of which is almost $3 \cdot 10^{-5}$ per avalanche carrier [4]. They can be re-absorbed within the substrate of the same SPAD and generate charge carriers able to travel to the active region and trigger a secondary avalanche. One way to limit optical afterpulse is using particular materials, like low-liftime substrate.

Crosstalk The crosstalk is a secondary noise which happens when multiple SPADs are lit by only one impinging photon. As previously mentioned, during each avalanche secondary photons are produced in an isotropic way. These photons can travel to neighbouring cells and trigger avalanches, resulting in "prompt" or "delayed" crosstalk, or they can exit on the active side of the SiPM and be reflected back by a protective window ("external" crosstalk).

Prompt crosstalk, not shown in Figure 2.10, happens when a secondary photon reaches another SPAD and makes the avalanche begin, hence it can be reduced by separating the cells via optical trenches. Given the small distance between the cells, there is almost no time delay between the primary and the secondary signal.

If the secondary photon is absorbed in the un-depleted region of a SPAD it can generate minority carriers which, diffusing to the multiplication region, can trigger an avalanche. This process is defined "delayed" crosstalk since usually the carriers diffusion time is long enough to have a discernible signal delay.

Generally, crosstalk can be minimized using low-gain SPADs, since producing less charges results in reducing the amount of secondary photons.

2.2.4 Photon Detection Efficiency

One of the most important performance parameters of a SiPM is the Photon Detection Efficiency (PDE), which measures the probability for an impinging photon to interact with a microcell and generate a detectable signal. It can be computed as [6]:

$$PDE(V_{ov}, \lambda) = QE(\lambda) \cdot P_T(V_{ov}, \lambda) \cdot FF \tag{2.5}$$

where QE is the quantum efficiency, P_T is the avalanche breakdown triggering probability and FF is the geometric fill factor. An example of possible dependence of the PDE from wavelength and overvoltage is shown in Figure 2.11.

Quantum efficiency The quantum efficiency is the probability that an impinging photon generates an electron-hole pair in the active region of the detector. It depends on two factors: the probability for the photon to cross the anti-reflective coating (a stack of dielectric layers) on the detector surface and the internal quantum efficiency, i.e. the probability of creating a carrier able to reach the high field region. Both of these quantities have a strong dependence on the photon's wavelength.

Avalanche triggering probability The triggering probability is the likelihood that a charge carrier moving through the high field region triggers an avalanche. It is linked to the triggering probabilities of electrons P_e and holes P_h by

$$P_T = P_e + P_h - P_e \cdot P_h \tag{2.6}$$

20

P_e and P_h are related to the impact ionization rates of the charge carriers, which increase with the electric field, subsequently P_T increases with the applied voltage. Moreover, the rate for electrons is higher than the one for holes, so the electrons are always more efficient in triggering avalanches.

Fill factor   The fill factor is the ratio between the active and the total area of the sensor. It is related to the presence of inactive areas needed to isolate the cells electrically and optically. In addition, it depends on the microcells size, ranging from 80% for 50x50 µm² SPADs to only 30% for 10x10 µm² SPADs.
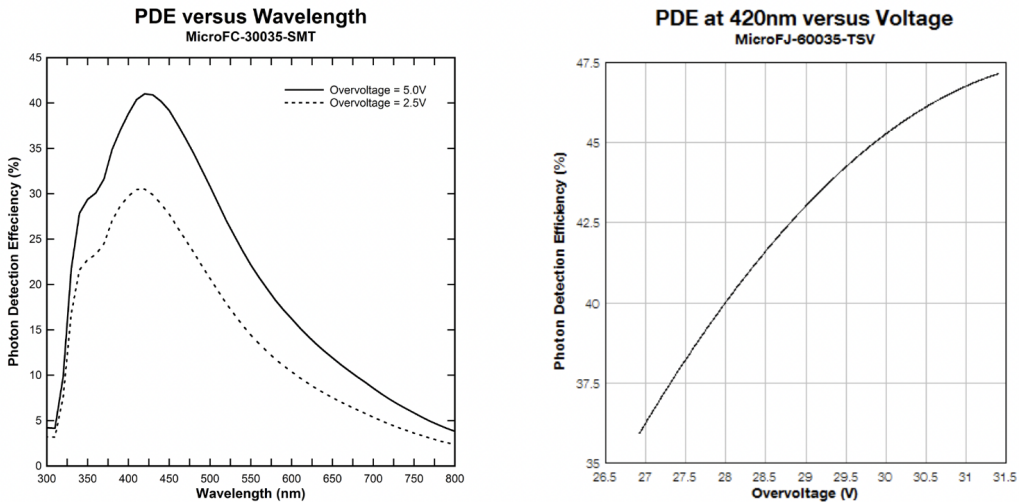

Figure 2.11: Photon Detection Efficiency as a function of wavelength (left) for different voltages and as a function of overvoltage for a 6 mm, 35 µm microcell SiPM, from [3].

2.2.5   Annealing

Particles travelling through the sensor can produce defects in its active volume. For example neutrons moving through the silicon can displace some atoms of the lattice, which subsequently form an agglomeration called "cluster". Macroscopically, bulk defects caused by radiation damage result in a deterioration of the sensor performance because their presence leads to an increase in the amount of generated charge carriers and thus in the dark current.

The SiPM performance can be recovered by means of thermal annealing, a process consisting in exposing the sensors to very high temperature whose effect is shown in Figure 2.12. The difficulties linked to realizing thermal annealing inside a detector can be overcome by inducing the process electrically, either in forward or reverse bias.
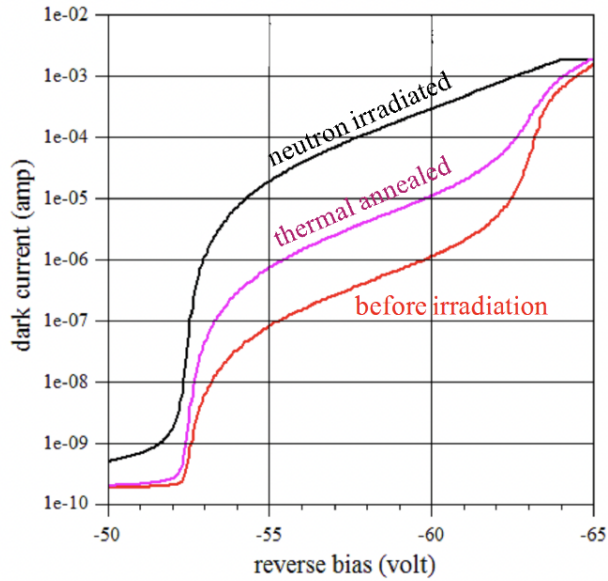
Figure 2.12: Dark current in a SiPM at room temperature, measured before and after irradiation and after an annealing cycle at 250 °C, from [7].

Apart from the possibility of recovering damaged sensors in-situ, another benefit of induced annealing is that the presence of an intense electric field can re-order the atoms which have been displaced by incoming radiation. Also, induced annealing can provide significant recovery in relatively small times. For example, Figure 2.13 shows the decrease of the dark current as a function of exposure time for experiments carried out on HAMAMATSU SiPMs [8].
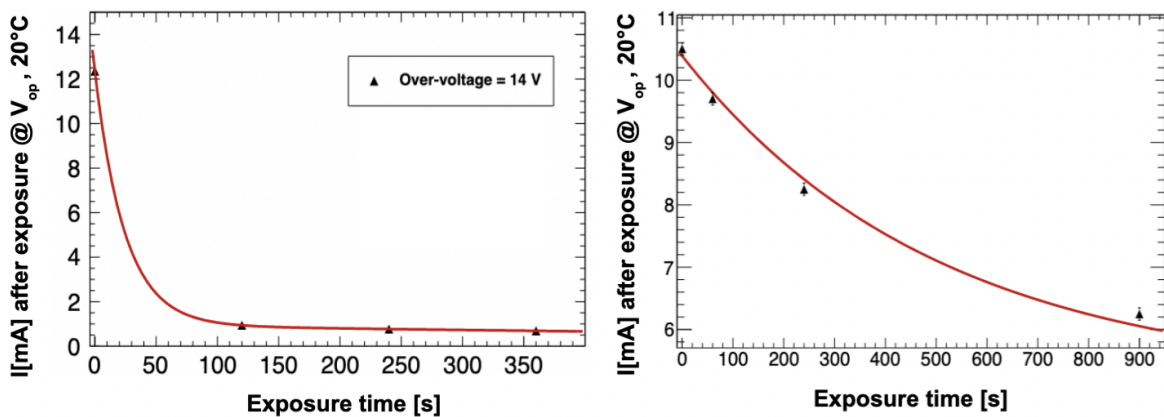

Figure 2.13: Dark current as a function of exposure time in HAMAMATSU SiPMs, in reverse (left) and forward (right) polarization, adapted from [8].

22

Chapter 3

Set-up study and SiPM characterisation

The aim of this work is the study of the set-up described in Section 3.1. It consists of a measurement apparatus with a pulsed LED light source used to test the light response of brand-new SiPM sensors kept at low temperature. This set-up can also be used to test irradiated or annealed sensors, in order to measure the changes in their light response. Section 3.2 covers the characterisation measurements of the light source, while Section 3.3 will describe the light response of sensors with 50x50 µm² cells.

3.1   Experimental Set-up

Since the SiPM dark current decreases strongly with temperature, the sensors have been operated inside a climatic chamber ENCO CTC-256 at a temperature of $-30\,°C$. The inside of the chamber, partially shown in Figure 3.1, contains:

- a LED light source, mounted on a sight;

- two boards on which the brand new HAMAMATSU 13360 SiPMs are mounted;

- an ALCOR chip [9] used to acquire data;

- an FPGA to read the ALCOR data;

- an X-Y movement system.

All the measurements on the SiPMs have been carried out at low temperature. However, since the movement system did not work correctly in this condition, in order to move from one sensor to the other it was necessary to undergo a temperature cycle (from $-30\,°C$ to $20\,°C$ and back to $-30\,°C$) which prolonged the time needed for the measurements.

The sensors are located on two boards, schematically depicted in Figure 3.2: a reference board (chip 0) containing a matrix of 4 SiPMs and a target board (chip 1) with 32 sensors. The presence of a reference board enabled us to periodically keep track of the measurement conditions stability by looking at the sensor A1. The target board alternates rows of 50 μm and 25 μm SiPMs, but because of the limited range of motion of the movement system only the rows from C to H were accessible. Every phase of the measurement procedure was automatized and could be controlled remotely.

The climatic chamber has a hole in the wall in order to let cables inside it. The external part of the measurement system is shown in Figure 3.3 and consists of:

- a AFG3252 pulse generator, which provides the pulses to the LED;

- a PHL250-P DC power supply used to bring high voltages to the sensors;

- an AIM-TTI QL355TP power supply used to give low voltages to the electronics;

- a KAESER DC 2.0 dryer used to have dry air circulation and limit humidity in the climatic chamber.

The LED pulses had a frequency of 100 kHz and a width of 5 ns.
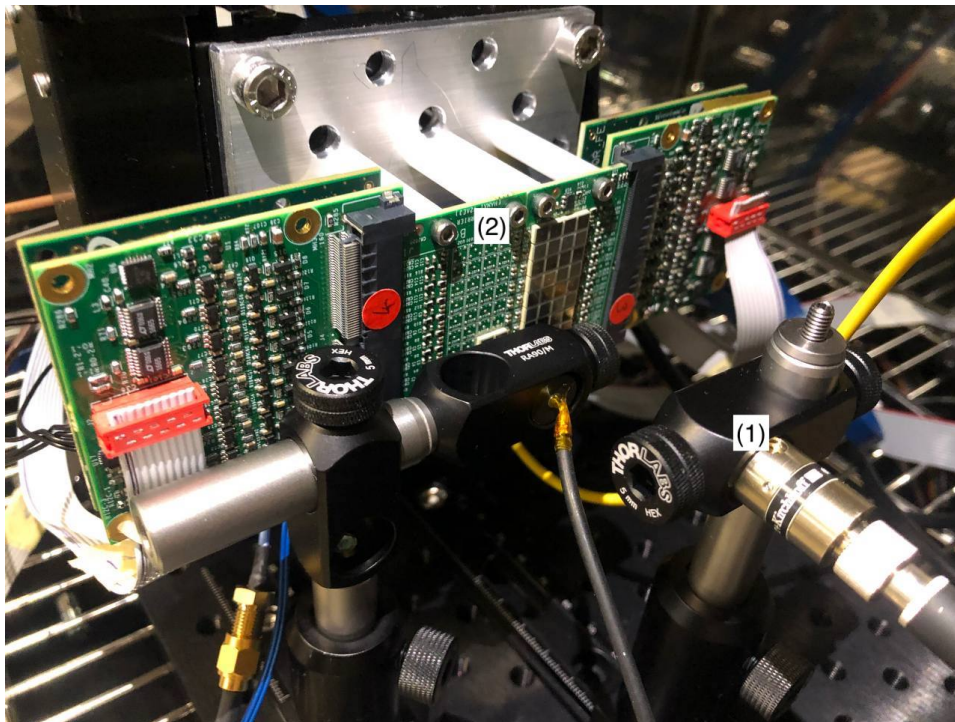

Figure 3.1: Part of the instrumentation inside the climatic chamber: LED light source (1) and device under test (2).
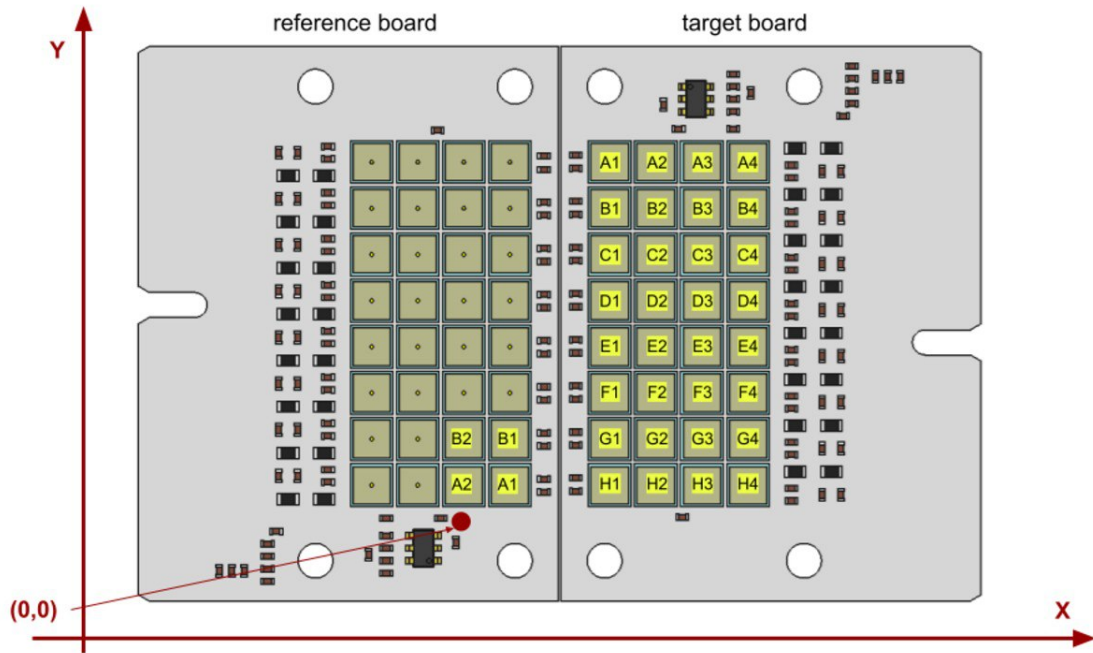
Figure 3.2: Illustration of the target and reference boards. The target board's only accessible rows are C, E and G for the 50 µm sensors and D, F, H for the 25 µm ones.
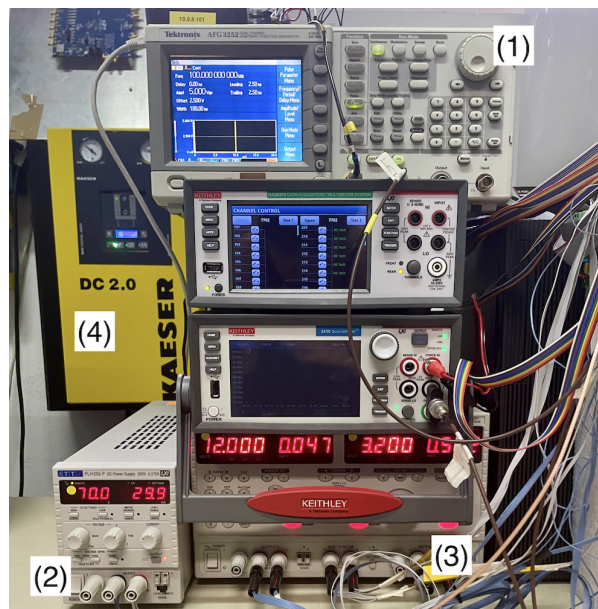

Figure 3.3: Measurement apparatus outside the climatic chamber: pulse generator (1), high (2) and low (3) voltage sources, air dryer system (4).

3.1.1 Device under test

In order to correctly characterise the SiPM response to impinging light it was necessary to take into account the DCR contribution to the output signal. To do so, every measurement has been carried out sequentially with the LED on and off. This gives the distribution of the dark count rate at the time of the measurement, which can be subtracted from the total output in order to obtain the rate of photon-generated events. Every measurement has been conducted repetitively in order to obtain a more detailed statistic. In every graph shown in the following the points are obtained as the average of all the corresponding measurements apart from the ones which were more than one standard deviation far from the mean value.

3.1.2 Movement system

The alignment of the movement system has been tested by taking rate measurements at room temperature while scanning some sensors in the X and Y directions. The resulting graphs, some examples of which are shown in Figure 3.4, have been fit with a function of the form

$$y = a \cdot 0.5 \cdot \left(1 - \mathrm{erf} \left(\frac{|x - x_m| - b}{c} \right) \right) \tag{3.1}$$

where erf is the error function, a is the height of the plateau, x_m is the spacial coordinate of the centre of the distribution, b is the half-width of the distribution and c is the width of the edges. The expected value of x_m for a correctly working system is zero.

Sensor	Direction	x_m (mm)
A1	X	-0.067 ± 0.011
	Y	-0.120 ± 0.012
C1	X	0.009 ± 0.011
	Y	-0.082 ± 0.011
C4	X	0.009 ± 0.012
	Y	-0.110 ± 0.012
G1	X	-0.046 ± 0.012
	Y	-0.052 ± 0.011
G4	X	-0.056 ± 0.011
	Y	-0.103 ± 0.011

Table 3.1: Mean value of the rate distribution fit function in position scans for different sensors.

In order to test the full XY range of the system, these measurements have been taken on the reference sensor A1 and on the outermost sensors on the lower (G) and higher
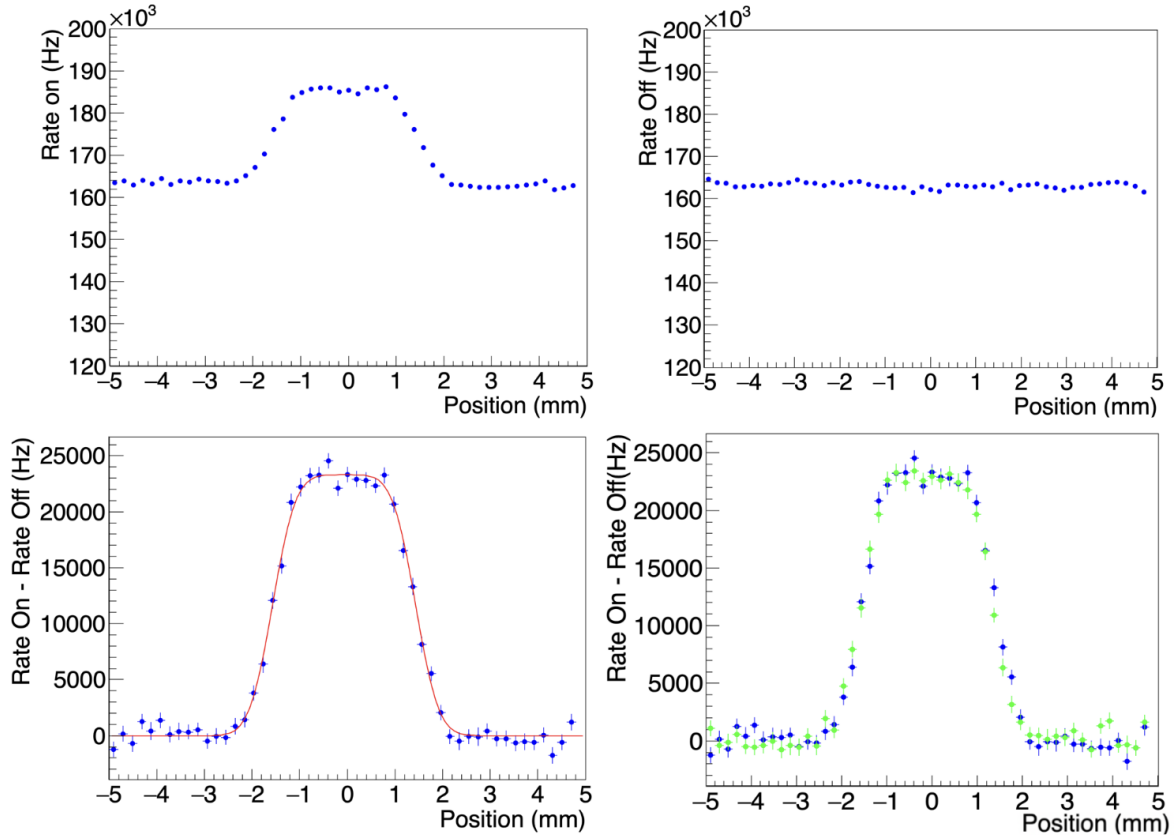
Figure 3.4: Rate measurements on sensor A1 for position scan in the X direction with the pulser on (up left) and off (up right). Fit of the rate distribution with Equation 3.1 (down left). Comparison between the X (blue) and Y (green) rate distributions (down right).

(C) reachable rows of $50\,\mu m$ SiPMs on the target board. The resulting values of x_m are presented in Table 3.1. Every sensor showed a distribution consistent with the expected one and symmetrical with respect to $x_m = 0$.

3.2 Light Source Characterization

3.2.1 Pulser Voltage

First of all, it was necessary to choose an adequate pulser voltage so that the light source would emit only one photon at a time. Although it is not possible to control the number of photons emitted by the LED, the condition can be met by minimizing the probability of emitting two or more photons.

In general, the probability of emitting n photons is described by the Poisson distribution

$$P(n; \lambda) = \frac{\lambda^n}{n!} e^{-\lambda} \qquad \forall n \in \mathbb{N} \tag{3.2}$$

where λ is the mean value. We wanted the distribution to have $\lambda^* = 0.02$ in order to have a difference of two orders of magnitude between the probability of having one photon and the one of having two. In fact, by setting $\lambda = \lambda^*$ in Equation 3.2 one finds $P(n = 1, \lambda^*) \sim 2 \cdot 10^{-2}$ and $P(n = 2, \lambda^*) \sim 2 \cdot 10^{-4}$.

In the practice the mean value of photons depends on the characteristics of the LED pulse, so we have performed measurements for different pulser voltages on the reference sensor A1 at a temperature $T = -30\,^{\circ}\mathrm{C}$ in order to find the value that better suited the condition provided above. The corresponding data are shown in Figure 3.5. The measured rate divided by the pulser rate (100 kHz) corresponds to the probability

$$P(n > 0; \lambda) = 1 - P(0; \lambda) = 1 - e^{-\lambda} \tag{3.3}$$

of detecting one or more photons, so in order to have a mean photons value of 0.02 the rate should be ~ 1.98 kHz. The corresponding pulser voltage is approximately $p_{vol} = 960$ mV, however every measurement described in the following paragraphs has also been performed at $p_{vol} = 980$ mV and $p_{vol} = 1000$ mV.
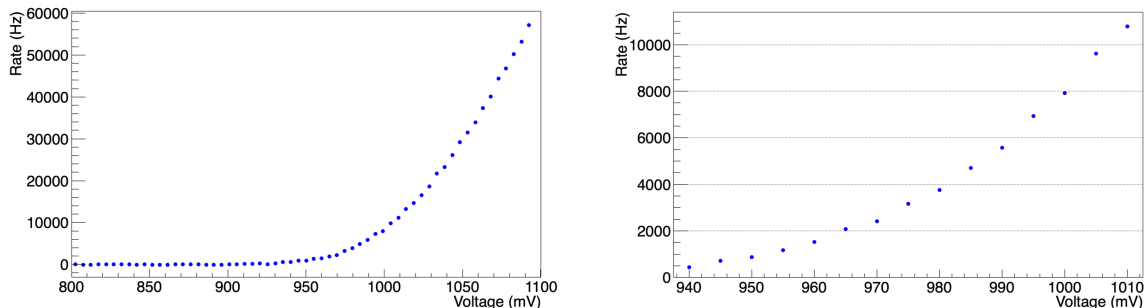

Figure 3.5: Difference between the rate with the pulser on and off on sensor A1 for different values of the pulser voltage. The figure on the right shows a more detailed scan in a smaller range of the variable.

3.2.2 Bias Voltage Scan

Figure 3.6 shows the dependence of the measured rate from the voltage V_{bias} applied to the reference sensor A1. As expected, when the bias voltage is too small the only detected signals are due to noise sources, while the output with the LED on becomes significantly different from the background at higher voltages.
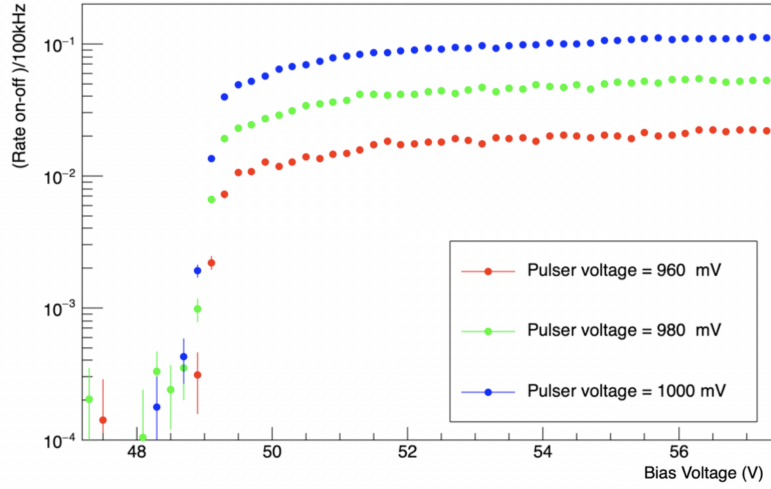
Figure 3.6: Dependence of the rate (on - off) on the applied voltage on sensor A1, for $p_{vol} = 960$ mV (red), $p_{vol} = 980$ mV (green), $p_{vol} = 1000$ mV (blue).
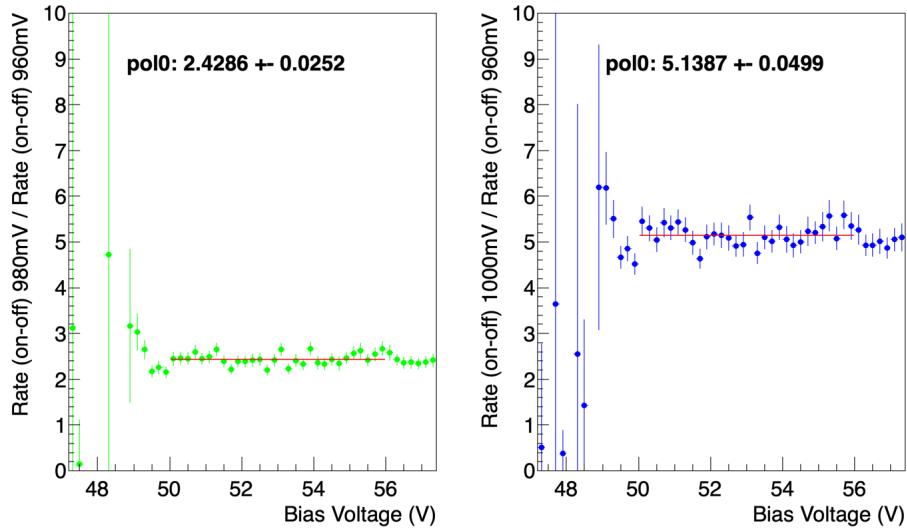

Figure 3.7: Dependence of the rate (on - off) on the applied voltage for $p_{vol} = 980$ mV (left) and $p_{vol} = 1000$ mV (right), normalized by the corresponding curve for $p_{vol} = 960$ mV. The red lines show the fit with a constant function for voltages between 50 and 56 V.

From a qualitative observation it can be noticed that the shape of the curve does not

depend on the quantity of light involved in the process, i.e. on the pulser voltage. This can be verified by normalizing the blue and the green curves to the red one, as shown in Figure 3.7. As expected, the ratio of two curves is well fit by a constant distribution, showing that they are one multiple of the other.

3.2.3   Threshold scan

The threshold scans on the reference sensor A1 shown in Figure 3.8 have been used to measure the probability of detecting multiple photons at a time, since the first plateau of the distribution corresponds to signals triggered by every possible number of events, while the second corresponds to signals due to only two or more triggering photons or noise events. In order to estimate this probability, the curves have been fit with two constant functions, one for each linear zone. The fit results are shown in Table 3.2.

p_{vol}	Pulser on		Pulser off	
	First plateau	Second plateau	First plateau	Second plateau
960 mV	$2616 \pm 15 \, \text{Hz}$	$216 \pm 4 \, \text{Hz}$	$1136 \pm 9 \, \text{Hz}$	$86 \pm 3 \, \text{Hz}$
980 mV	$4910 \pm 19 \, \text{Hz}$	$413 \pm 6 \, \text{Hz}$	$1170 \pm 10 \, \text{Hz}$	$89 \pm 3 \, \text{Hz}$
1000 mV	$8940 \pm 30 \, \text{Hz}$	$854 \pm 8 \, \text{Hz}$	$1140 \pm 10 \, \text{Hz}$	$86 \pm 2 \, \text{Hz}$

Table 3.2: Rate in the first and second plateaus of the threshold scan distributions obtained by fitting with a constant function.

The probability $P(n > 0; \lambda)$ can be evaluated as the difference in height between the first plateaus of the distributions with the LED turned on and off, normalized by the pulser rate. This probability can be used to evaluate λ with Equation 3.3, the results are shown in Table 3.3. The table also indicates the expected rate of events triggered by two or more photons for the given values of λ, evaluated using Equation 3.2 and multiplying by the pulser rate.

p_{vol}	λ	$P(n > 1; \lambda) \cdot 100\text{kHz}$
960 mV	0.0148 ± 0.0002	10.8 ± 0.3 Hz
980 mV	0.0380 ± 0.0002	70.4 ± 0.8 Hz
1000 mV	0.0811 ± 0.0003	312 ± 2 Hz

Table 3.3: Measured mean value of photons λ and "theoretical" rate of events involving more than one photon.

The expected rate of multiple photon events can be compared to the scaling between the second plateaus of the pulser on and pulser off distributions. In order to compare

these two numbers, however, the contribution of crosstalk events should be taken into account. The crosstalk probability P_x can be evaluated as the ratio of the second to first plateau with no impinging light, since in that case multiple events can only be triggered by crosstalk between cells. The rate R_2 of events triggered by multiple photons, subsequently, is the difference between the plateaus scaling and the crosstalk rate. As shown in Table 3.4, the measured rate of multiple photons events is smaller than the expected one in two cases out of three; this can be probably due to the presence of afterpulses which increase the dark count rate.
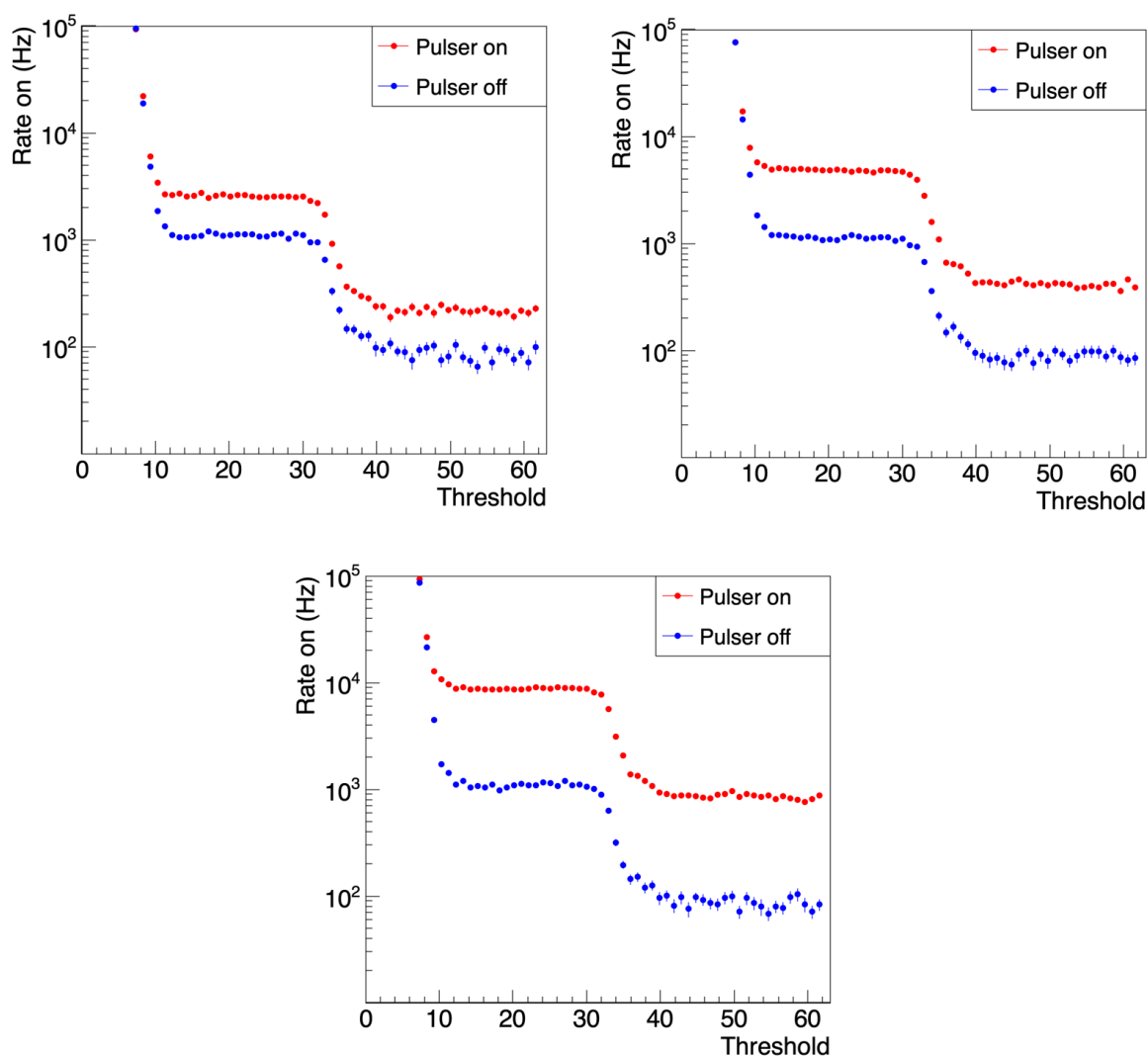
Figure 3.8: Dependence of the rate from the threshold value with the pulser on (red) and off (blue) for $p_{vol} = 960$ mV (up left), $p_{vol} = 980$ mV (up right) and $p_{vol} = 1000$ mV (down).

| p_{vol}	P_x	Crosstalk rate	R_2
960 mV	0.075 ± 0.003	$111 \pm 6\,\mathrm{Hz}$	$19 \pm 11\,\mathrm{Hz}$
980 mV	0.076 ± 0.003	$284 \pm 14\,\mathrm{Hz}$	$40 \pm 20\,\mathrm{Hz}$
1000 mV	0.076 ± 0.002	$590 \pm 20\,\mathrm{Hz}$	$180 \pm 30\,\mathrm{Hz}$

Table 3.4: Crosstalk rate and probability in the three pulser voltage configurations, rate of events triggered by more than one photon.

3.2.4 Stability

In order to verify the stability of the measurement conditions, we have carried out a scan for a time frame longer than 24 h. Data were collected for three different values of the pulser voltage (960, 980 and 1000 mV) and three different bias voltages (51.3, 52.3 and 53.3 V), repeating the measure 101 times for each configuration. Figure 3.11 shows the measured rate as a function of time fit with a constant function. In each configuration the $\tilde{\chi}^2$ is small enough to assert that the measurement is stable.

Data collected in this scan have also been used to check whether the temperature oscillations in the climatic chamber could affect the measurements. Although the data shown in Figure 3.12 show a trend with the temperature, the rate change in the considered range is negligible.
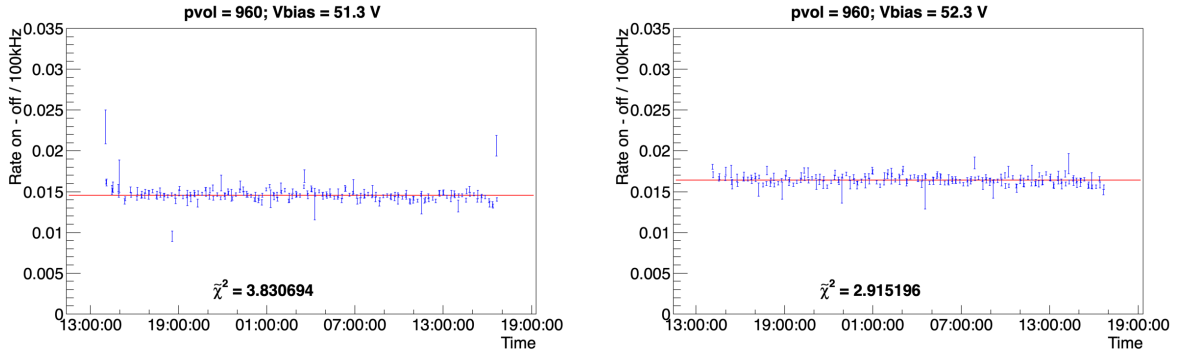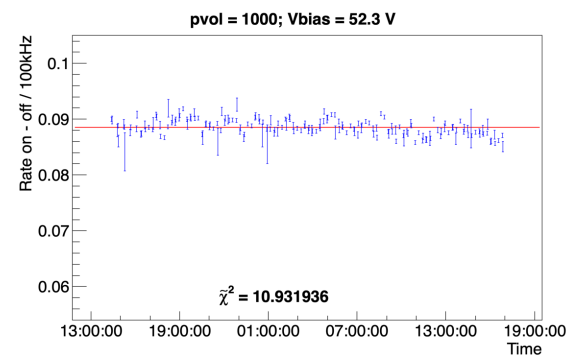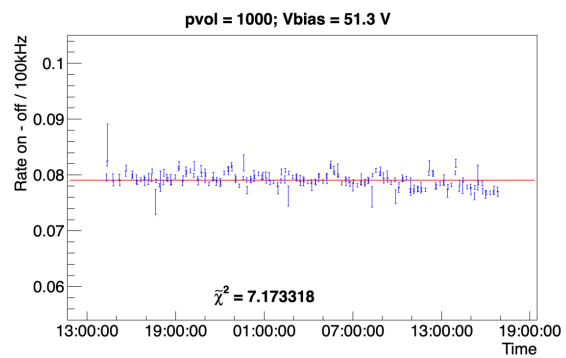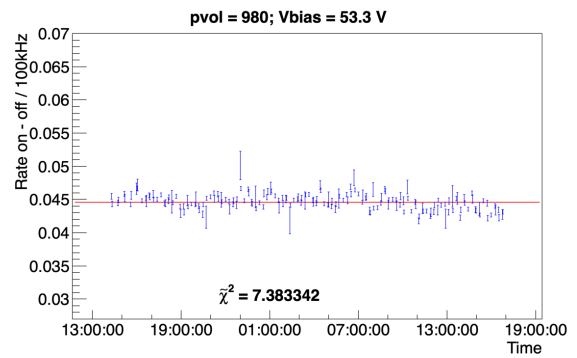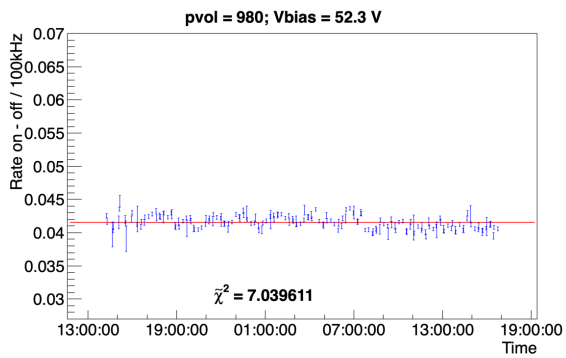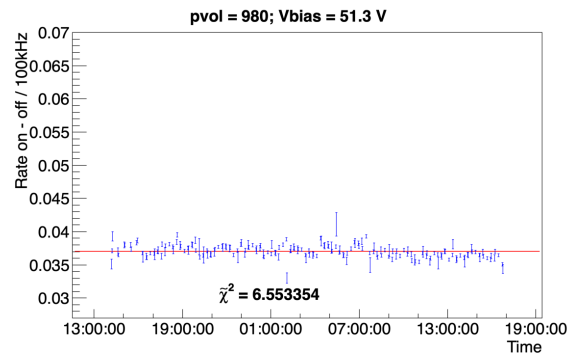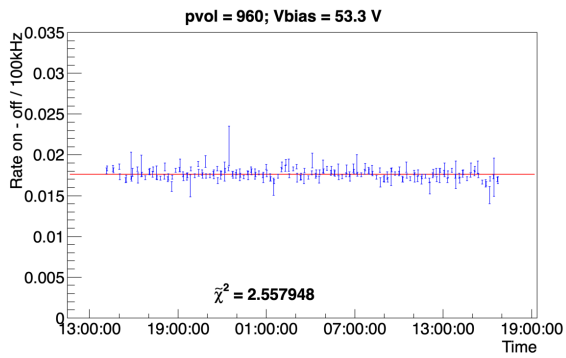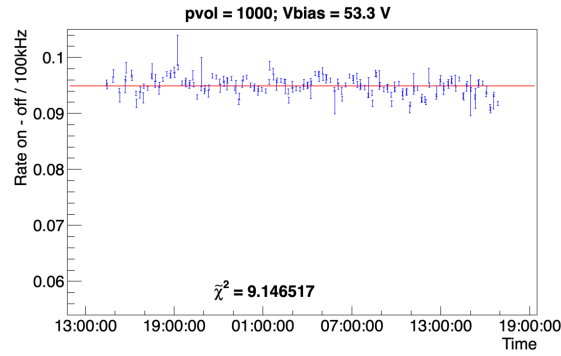
Figure 3.11: Rate as a function of time for a time interval of more than 24 h in different configurations, reduced chi-squared values of the corresponding constant fits.
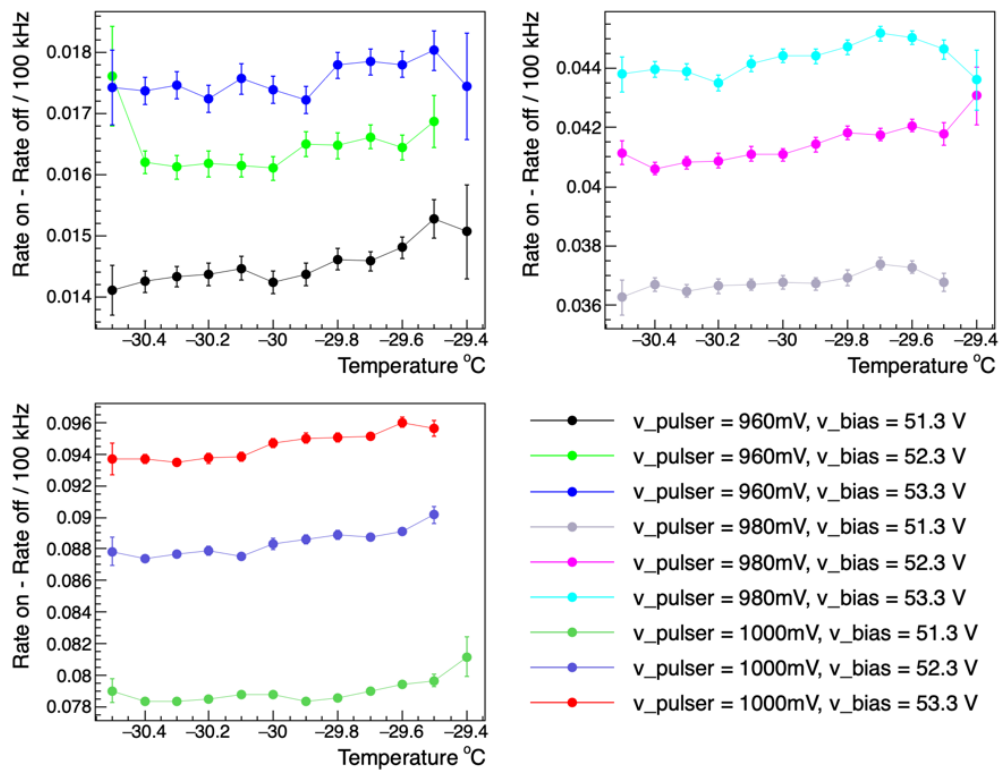

Figure 3.12: Temperature dependence of the rate in different configurations.

3.3 Board Scan: Sensors Consistency

After characterising the light source, we started to collect data on the target board's $50\,\mu\text{m}$ sensors. In order to keep track of the stability of the measurement conditions it was necessary to cross-check periodically with the reference sensor A1, therefore the scan procedure was:

1. characterise the pulser light on A1;

2. scan the first row of sensors (C);

3. measure A1 to check whether the measurement conditions are stable;

4. scan the second row of sensors (E);

5. repeat the measure on A1;

6. scan the last row of sensors (G).

These measurements covered a time frame of one week, during which the reference sensor has been measured several times.

3.3.1 Reference sensor

The threshold and V_{bias} scans taken on A1 during this period are shown in Figure 3.13 and Figure 3.14, respectively.
Having a lot of data on the same sensor can be used to evaluate the dispersion associated to repeated measurements. To do so we compared the V_{bias} data with their mean and associated to each configuration a total dispersion based on the dispersion of this distribution, an example of which is shown in Figure 3.15.
The total dispersion can be furthermore broken down in two components:

- statistical fluctuations due to the measurement uncertainty;

- systematic fluctuations due to the uncertainty in the measurement reproducibility.

The statistical contribution has been evaluated by averaging the statistical errors of each point, while the systematic dispersion was obtained as the square difference between the total dispersion and the statistical error. The results of these calculations are shown in Figure 3.16.
The mean value of the systematic dispersion is $\sim 3.4\%$ for $V_{threshold} + 3$ and $\sim 3.2\%$ for $V_{threshold} + 5$, which means that the set-up is stable within these errors.

3.3.2 Target board

Figure 3.17 and Figure 3.18 depict the threshold and V_{bias} scans performed on the SiPMs in the rows C, E and G of the target board.

As expected, the dependence of the rate from the bias voltage is the same for each sensor. Hence the systematic dispersion can be evaluated using the same method as before, but it should be further divided in two contributions: the systematic fluctuation on reproducibility, measured on sensor A1, and an additional component due to sensors inhomogeneity. As a result, the total dispersion is higher compared to the one on sensor A1.

The different contributions to the total dispersion are shown in Figure 3.19, where an unexpected dependence of the systematic error from the pulser voltage can be noticed. A possible cause for this behaviour could be that the LED light has different wavelengths for different voltages, thus the sensors might have a different efficiency in detection. However, since the climatic chamber was unavailable, it was not possible to test this hypothesis.
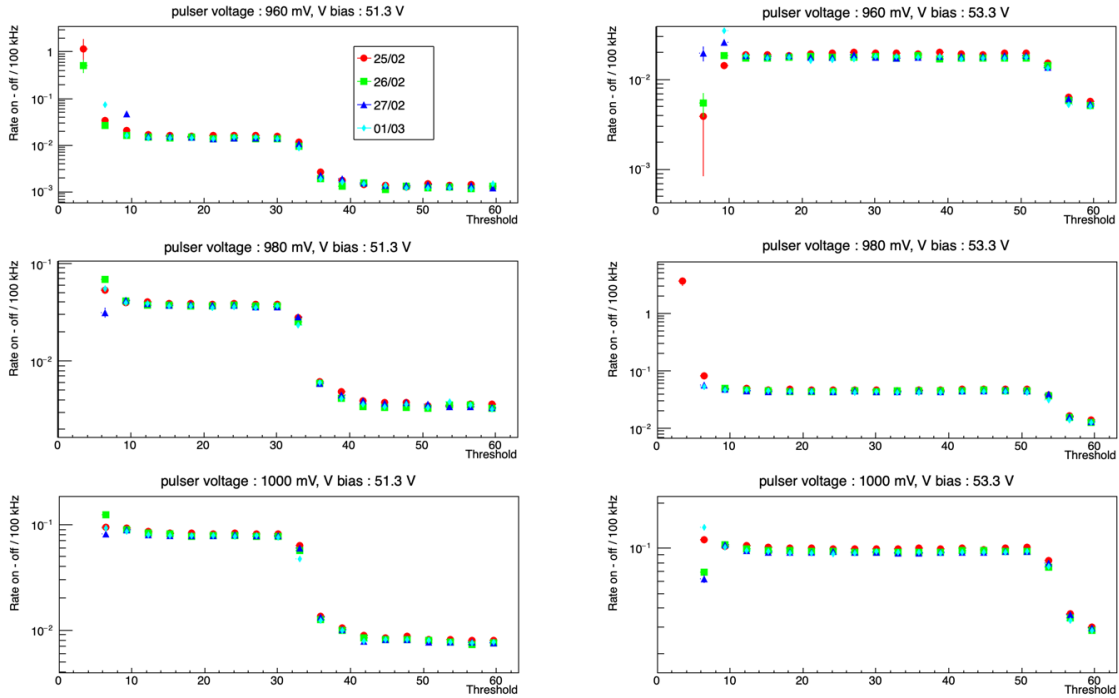

Figure 3.13: Threshold scans on the reference sensor A1 in different days and for different values of the pulser voltage and the bias voltage.
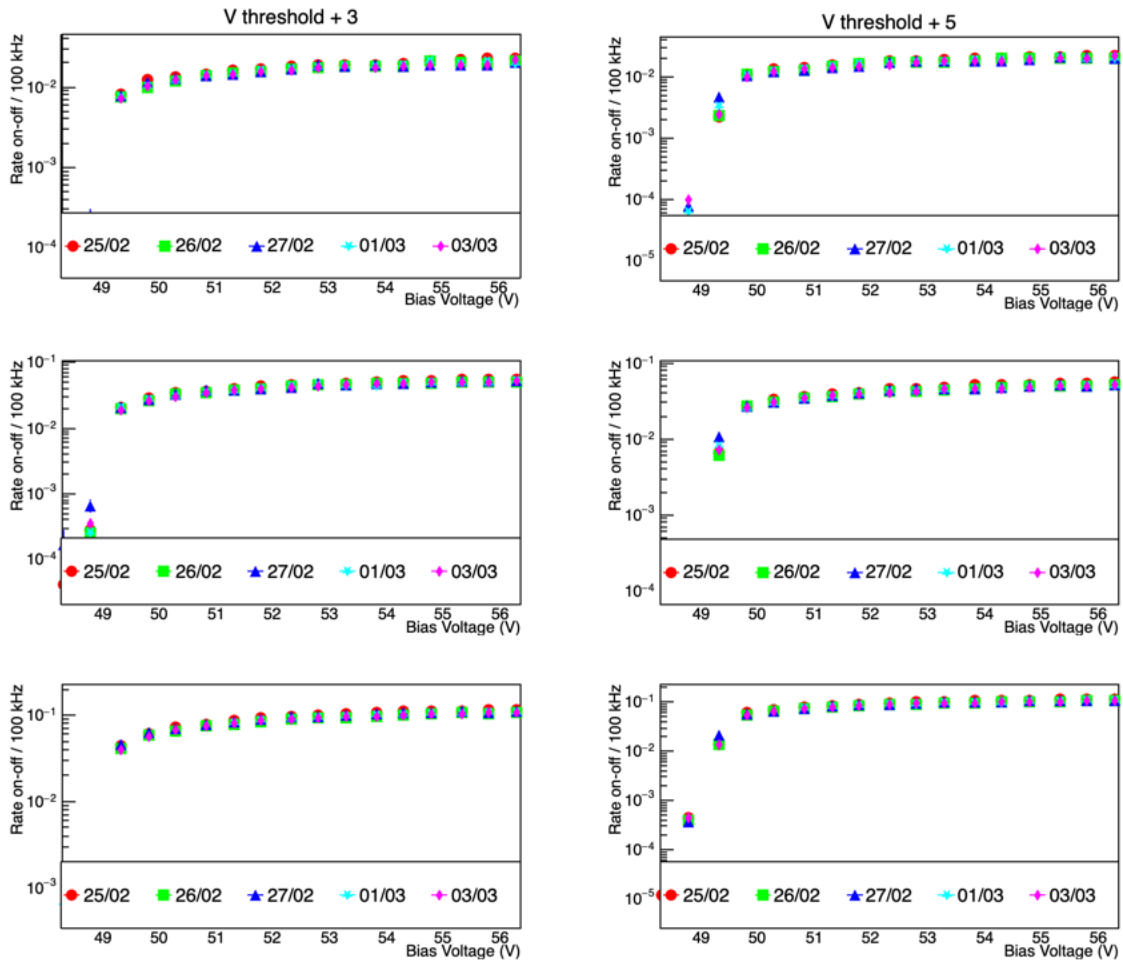
Figure 3.14: V_{bias} scans on reference sensor A1 in different days. The pulser voltage is 960 mV in the upper row, 980 mV in the middle row and 1000 mV in the lower row.
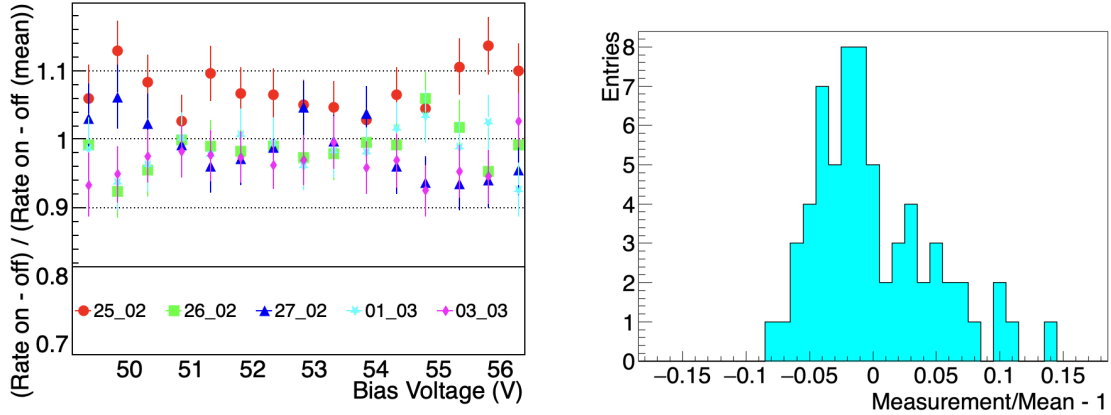
Figure 3.15: V_{bias} curves of sensor A1 normalized to their mean value (left), distribution of the ratios between the measurements and their mean value (right). Both figures represent the configuration $p_{vol} = 960$ mV, $V_{threshold} + 3$.
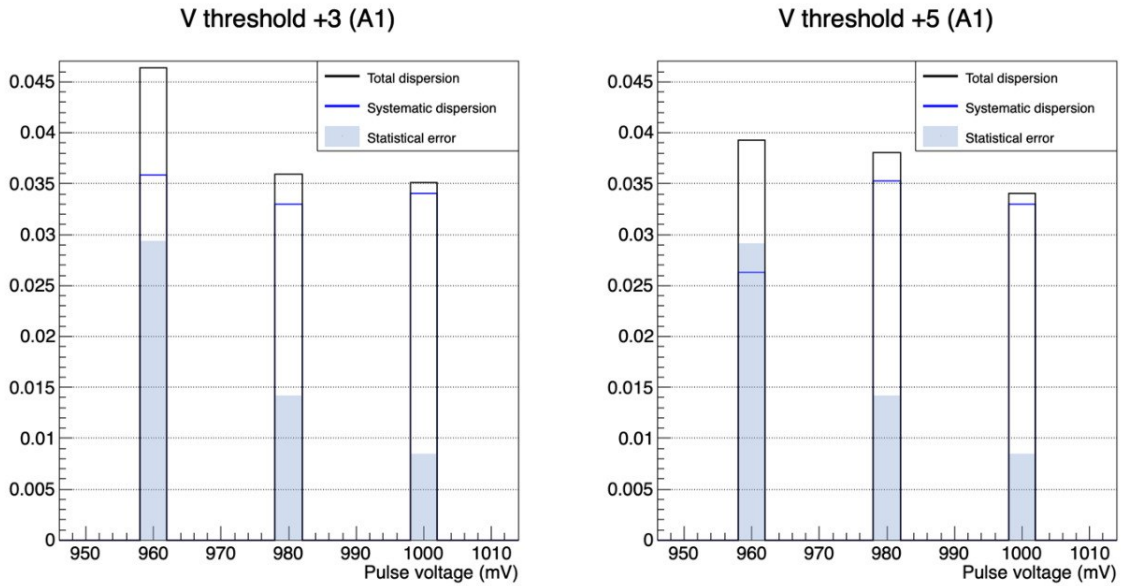

Figure 3.16: Total, statistical and systematic dispersions of V_{bias} measurements on the reference sensor A1, for $V_{threshold} + 3$ (left) and $+ 5$ (right).
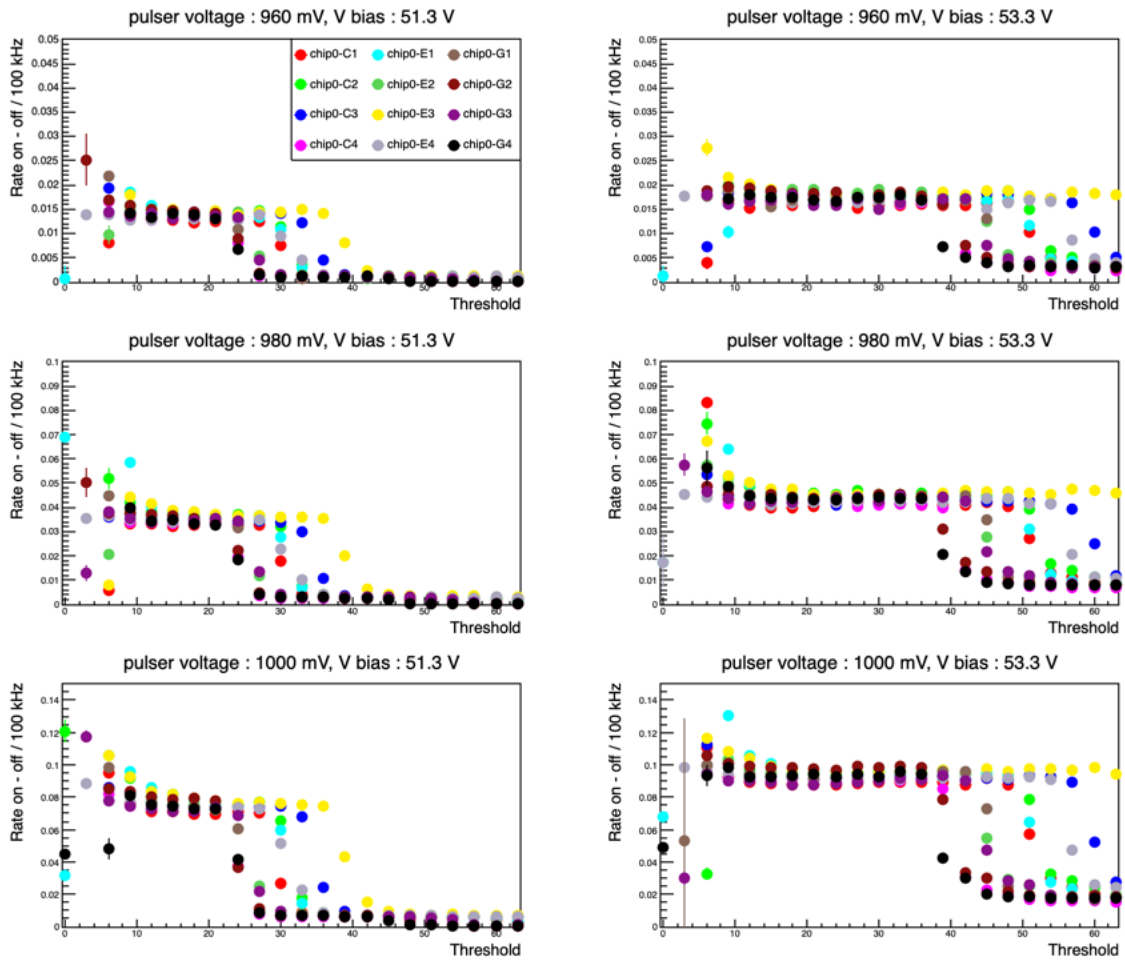
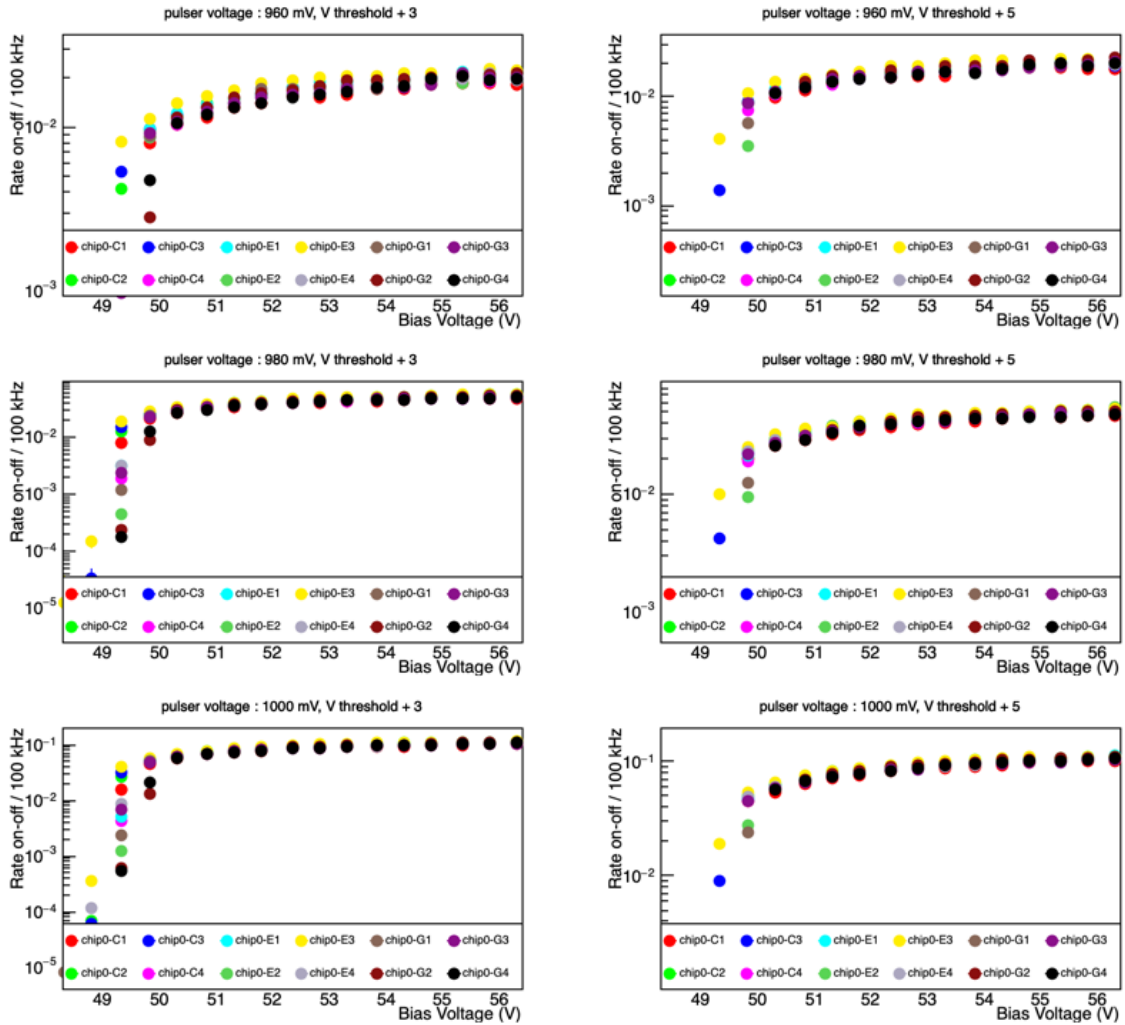Figure 3.17: Threshold scans on the 50 µm SiPMs in rows C, E and G in different configurations.

Figure 3.18: V_{bias} scans on the $50\,\mu m$ SiPMs in rows C, E and G in different configurations.
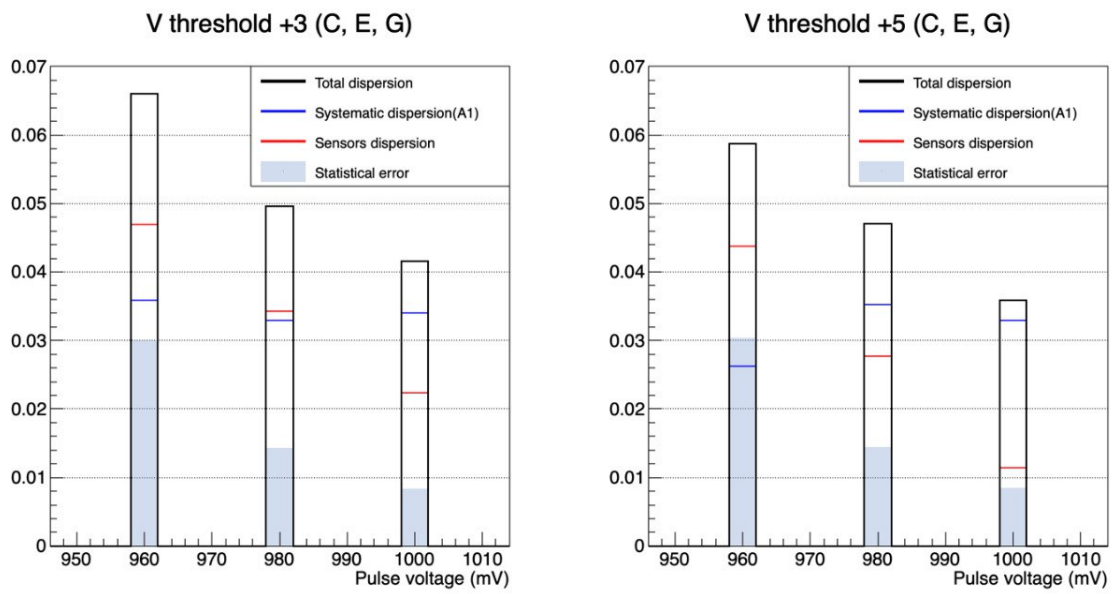
Figure 3.19: Total, statistical and systematic dispersions of V_{bias} measurements on the tested SiPMs, for $V_{threshold} + 3$ (left) and $+ 5$ (right). The systematic dispersion is broken down into a contribution due to the measurement repeatability and one due to the sensors inhomogeneities.

Conclusions

The aim of this work was to study and to assess the proper functionality and stability of a pulsed LED set-up to characterise the light response of SiPM sensors at a temperature $T = -30\,°\text{C}$.

After verifying the correct positioning of the movement system, we carried out measurements in order to characterise the LED light source. From a preliminary analysis, we found the best value for the pulser voltage in order to limit the rate of events triggered by more than two photons. This corresponds to a Poisson distribution with mean $\lambda = 0.02$, realized approximately at $p_{vol} = 960\,\text{mV}$. Observations on the threshold scans of a reference sensors enabled us to measure the value of λ and the corresponding rate of events involving multiple photons. However, this rate has been found to be smaller than the one evaluated assuming a Poisson distribution of emitted photons, probably due to the effect of afterpulses.

We checked the measurement stability collecting data for a long time interval, ensuring that the rate remained approximately constant independently from the time passing and the temperature shifts inside the climatic chamber.

Afterwards we began to characterise the light response of brand new SiPMs, with the aim of moving to irradiated sensors subsequently, but after a blackout the climatic chamber stopped working and was unavailable for two months, preventing to collect data on irradiated sensors. Subsequently the only available data were the ones regarding the 50 µm brand-new sensors. These data have been used to quantify the measurement repeatability by looking at the dispersion of the same measurement among different sensors. We found a systematic dispersion of approximately 3.5% independently from the LED conditions, which should be added to the contribution due to the sensors inhomogeneity in order to obtain the total systematic dispersion.

Bibliography

[1] A. Accardi *et al.*, "Electron Ion Collider: The Next QCD Frontier - Understanding the glue that binds us all," 2012. `https://arxiv.org/abs/1212.1701`.

[2] R. Abdul Khalek *et al.*, "Science Requirements and Detector Concepts for the Electron-Ion Collider: EIC Yellow Report," 2021. `https://arxiv.org/abs/2103.05419`.

[3] SensL, "An Introduction to the Silicon Photomultiplier." `https://elearning.unimib.it/pluginfile.php/521118/mod_folder/content/0/SiPM.pdf`.

[4] S. Gundacker and A. Heering, "The silicon photomultiplier: fundamentals and applications of a modern solid-state photon detector," *Physics in Medicine & Biology*, vol. 65, p. 17TR01, aug 2020. `https://doi.org/10.1088/1361-6560/ab7b2d`.

[5] T. Masuda *et al.*, "Suppression of the optical crosstalk in a multi-channel silicon photomultiplier array," *Optics Express*, vol. 29, p. 16914, may 2021. `https://arxiv.org/abs/2105.01519`.

[6] C. Piemonte and A. Gola, "Overview on the main parameters and technology of modern Silicon Photomultipliers," *Nuclear Instruments and Methods in Physics Research Section A: Accelerators, Spectrometers, Detectors and Associated Equipment*, vol. 926, pp. 2–15, 2019. `https://www.sciencedirect.com/science/article/pii/S0168900218317716`.

[7] T. Tsang, T. Rao, S. Stoll, and C. Woody, "Neutron radiation damage and recovery studies of SiPMs," *Journal of Instrumentation*, vol. 11, pp. P12002–P12002, dec 2016. `https://doi.org/10.1088/1748-0221/11/12/p12002`.

[8] M. Cordelli, E. Diociaiuti, A. Ferrari, S. Miscetti, S. Müller, G. Pezzullo, and I. Sarra, "An induced annealing technique for SiPMs neutron radiation damage," *Journal of Instrumentation*, vol. 16, p. T12012, december 2021. `https://doi.org/10.1088/1748-0221/16/12/T12012`.

[9] M. Rolo and F. Cossio, "The ALCOR ASIC for EIC applications," december 2021. `https://agenda.infn.it/event/28762/contributions/146408/attachments/87284/116576/20211121_ALCOR4EIC.pdf`.